SIMULATING THE DIURNAL CYCLE OF THE ATMOSPHERIC BOUNDARY LAYER USING LARGE-EDDY SIMULATION WITH VERTICAL ADAPTIVE MESH REFINEMENT

by

Nathan F. Andrews

A thesis submitted to the faculty of
The University of Utah
in partial fulfillment of the requirements for the degree of

Master of Science

Department of Mechanical Engineering

The University of Utah

August 2012

The University of Utah Graduate School

STATEMENT OF THESIS APPROVAL

The thesis of **Nathan F. Andrews**

has been approved by the following supervisory committee members:

James R. Stoll II	, Chair	**06/13/12** Date Approved
Eric R. Pardyjak	, Member	**06/08/12** Date Approved
Meredith M. Metzger	, Member	**06/14/12** Date Approved

and by **Timothy Ameel**, Chair of the Department of **Mechanical Engineering**

and by Charles A. Wight, Dean of The Graduate School.

ABSTRACT

The diurnal evolution of the atmospheric boundary layer (ABL) plays an important role in weather, climate systems and particle and pollutant transport. Many numerical studies break the diurnal cycle up into its two primary components, the daytime convective period and the nocturnal stable period and only recently into the morning and evening transitions. This is especially prevalent in large-eddy simulation (LES) studies where simultaneously representing the diurnal cycle's two distinct regimes creates domain size and resolution problems. During the daytime, when positive buoyancy forces result in a rapidly growing boundary layer with highly energetic, large-scale turbulence, the domain size must be large enough to capture these motions. In contrast, at night negative buoyancy forces suppress turbulence resulting in a much lower boundary layer height and significant small-scale turbulent fluxes necessitating a finer grid resolution. While both regimes have been modeled successfully in independent simulations, most diurnal cycle LES studies under resolve the nocturnal boundary layer in order to capture the large-scale features of the convective boundary layer. Here, LES is combined with adaptive mesh refinement (AMR) in the vertical direction to achieve a more efficient and robust simulation of the diurnal ABL. Vertical grid spacing is adjusted with relocation-type refinement (r-refinement) to provide increased vertical resolution in the boundary layer without adding the computational overhead of additional points. Simulations of the 24-hour Wangara case (days 33/34) demonstrate that LES with AMR can successfully adapt in space and time to changing turbulent length scales, providing increased resolution within the boundary layer and improved results compared to simulations with a static grid and the same total number of grid points. During the daytime convective period, increased resolution in near surface and entrainment regions leads to better-represented first and second order statistics. During the nocturnal period, AMR simulations cluster grid points within the boundary layer improving the representation of stratified turbulence. While the representation of the nocturnal boundary layer is improved, results highlight the importance of employing sufficient resolution, especially in the horizontal direction, during highly stratified periods.

CONTENTS

ABSTRACT . . . . . **iii**

LIST OF FIGURES . . . . . **v**

LIST OF TABLES . . . . . **viii**

ACKNOWLEDGMENTS . . . . . **ix**

CHAPTERS

1. INTRODUCTION **1**

2. ADAPTIVE MESH REFINEMENT **4**

2.1 AMR combined with LES in general 5
2.2 AMR used in ABL simulations 6

3. NUMERICAL SIMULATION **8**

3.1 LES methods 8
3.2 AMR method 9
3.2.1 AMR numerics 11
3.2.2 Monitor function 12
3.3 Case description 13
3.3.1 Initial conditions, boundary conditions, and forcings 13
3.4 Resolutions and simulations 14
3.4.1 Computational costs 16

4. RESULTS AND DISCUSSIONS **18**

4.1 Comparison to Wangara data 18
4.2 AMR behavior 24
4.3 Convective regime 26
4.4 Stable regime 38

5. CONCLUSIONS **47**

APPENDIX: AMR CRITERIA COMPARISON **50**

REFERENCES **58**

LIST OF FIGURES

3.1 Time series of the potential temperature and moisture screen measurements [28]. 15

3.2 Time-height contours for geostrophic winds: streamwise (left) and spanwise (right) [106]. 15

4.1 Time-height contours for LES 192^3 results (top) versus Wangara data (bottom) for mean wind speed (left) and potential temperature (right). 19

4.2 Comparison of plane averaged, instantaneous vertical profiles for LES 192^3 (a,b) versus instantaneous Wangara data (c,d). Mean wind speed (a,c) and potential temperature (b,d) are provided for the convective regime. Line types are as follows: 1100 LST (——), 1200 LST (– · –), 1300 LST (– –), 1400 LST (· · · · ·), 1500 LST (▬▬), 1600 LST (▬ · ▬). 21

4.3 Comparison of plane averaged, instantaneous vertical profiles for LES 192^3 (a,b) versus instantaneous Wangara data (c,d). Mean wind speed (a,c) and potential temperature (b,d) are provided for the stable regime. Line types are as follows: 2100 LST (——), 0000 LST (– · –), 0300 LST (– –),0600 LST (· · · · ·) 22

4.4 Time series obtained from 192^3 LES. boundary layer height, BLH (a), surface sensible heat flux, $\langle w\theta \rangle_0$ (b), surface friction velocity, u_* (c), Obukhov length, L (d), wind direction near the ground, α_0 (e), and wind direction at approximately 100 m, α_{100} (f) 23

4.5 Behavior of the AMR criteria of Eq. (3.18). The contour plot shows vertical resolution (m) profiles every 5 minutes. The LES computed boundary layer height (——)is overlaid for reference excluding the transitions. 25

4.6 Comparisons of the LES time series of boundary layer height, z_i (a), surface sensible heat flux, $\langle w\theta \rangle_0$ (b), surface friction velocity, u_* (c), and wind direction, α_0 (d) with corresponding Clarke data ($C71_0$). Line types are as follows: AMR (– –), 96^3 (– · –), 192^3 (——), H81(▪), and $C71_0$(•). 27

4.7 Comparison of LES u, (a,c,e) and v (b,d,f), velocity components during the convective regime. Hourly averages are from top to bottom: 1300-1400 LST (a,b), 1400-1500 LST (c,d), and 1500-1600 LST (e,f). Line types are as follows: AMR (– –), 96^3 (– · –), 192^3 (——). 29

4.8 Comparison of LES θ (a,c,e) and total sensible heat flux $\langle w\theta \rangle$ (b,d,f) during the convective regime. Hourly averages are from top to bottom: 1300-1400 LST (a,b), 1400-1500 LST (c,d), and 1500-1600 LST (e,f). Line types are as follows: AMR (– –), 96^3 (– · –), 192^3 (——). 30

4.9 Comparison of LES nondimensional total sensible heat flux $\langle w\theta \rangle \langle w\theta \rangle_0^{-1}$ during the convective regime. An insert is provided to enlarge the entrainment zone. Hourly average is for 1400-1500 LST. Line types are as follows: AMR (– –), 96^3 (– · –), 192^3 (——). 32

4.10 Comparison of LES total horizontal variances $\sigma_h w_*^{-2}$ (a,c,e) and vertical variance $\sigma_w w_*^{-2}$ (b,d,e) during the convective regime. Hourly averages are from top to bottom: 1300-1400 LST (a,b), 1400-1500 LST (c,d), and 1500-1600 LST (e,f). Line types are as follows: AMR (– –), 96^3 (– · –), 192^3 (——), $96 \times 96 \times 192$ (– · –). Thick lines are SGS vertical variance contribution. 34

4.11 Comparison of LES total potential temperature variance $\sigma_\theta \theta_*^{-2}$ (a) and LES resolved vertical velocity skewness $\langle w^3 \rangle \langle w^2 \rangle^{-3/2}$ (b) during the convective regime. An insert is provided to enlarge the entrainment regions of the potential temperature variance. The hourly average of both plots is between 1400-1500 LST. Line types are as follows: AMR (– –), 96^3 (– · –), 192^3 (——), $96 \times 96 \times 192$ (– · –) 36

4.12 Comparisons of the LES time series for the stable regime of boundary layer height, H (a), surface sensible heat flux, $\langle w\theta \rangle_0$ (b), surface friction velocity, u_* (c), Obukhov length, and near surface wind direction, α with corresponding Clarke data $C71_0$. Line types are as follows: AMR (– –), 96^3 (– · –), 192^3 (——), $96 \times 96 \times 192$ (– · –), H81(▪), and $C71_0$(•). 39

4.13 Comparison of LES mean wind speed and total momentum flux during the stable regime. Hourly averages are between 2000-2100 LST (a,b), 2300-2400 LST (c,d), and 0200-0300 LST (e,f). Line types are as follows: AMR (– –), 96^3 (– · –), 192^3 (——), $96 \times 96 \times 192$ (– · –) 40

4.14 Comparison of LES potential temperature, θ (a,c,e) and sensible heat flux, $\langle w\theta \rangle$ (b,d,f). Hourly averages are between 2000-2100 LST (a,b), 2300-2400 LST (c,d), and 0200-0300 LST (e,f). Line types are as follows: AMR (– –), 96^3 (– · –), 192^3 (——), $96 \times 96 \times 192$ (– · –) 42

4.15 Comparison of LES normalized momentum flux $u_{*L}^2 u_*^{-2}$ (a) and normalized sensible heat flux, $\langle w\theta \rangle \langle w\theta \rangle_0^{-1}$ (b,c) during the stable regime. Plot (a) contains profiles averaged between 2000-2100 LST, 2300-2400 LST, and 0200-0300 LST. Plot (b) contains profiles averaged between 2000-2100 LST and 2300-2400 LST. Plot (c) contains profiles averaged between 0200-0300 LST. Line types are as follows: AMR (– –), 96^3 (– · –), 192^3 (——), $96 \times 96 \times 192$ (– · –), and Nieuwstadt [73] (•——•) 44

4.16 Comparison of SGS (thin lines) and resolved contributions (thick lines) to LES normalized momentum flux $u_{*L}^2 u_*^{-2}$ (a,b) and normalized sensible heat flux, $\langle w\theta \rangle \langle w\theta \rangle_0^{-1}$ (c) during the stable regime. Hourly average is between 2300-2400 LST. Line types are as follows: AMR (– –), 96^3 (– · –), 192^3 (——), $96 \times 96 \times 192$ (– · –). 46

A.1 Behavior of three different AMR criteria. Contour plots show vertical resolution (m) profiles saved every 5 minutes of physical time. Boundary layer heights are overlaid to show turbulence regimes. Criteria are detailed in Table A.1. 51

A.2 Comparisons of the LES time series of boundary layer height, z_i (a), surface sensible heat flux, $\langle w\theta \rangle_0$ (b), surface friction velocity, u_* (c), and wind direction, α (d) with corresponding Clarke data ($C71_0$). Line types are as follows: criteria (a) (– –), criteria (b) (– · –), criteria (c) (– · –), 192^3 (——). H81(▪), $C71_0$(•). 53

A.3 Comparison of LES potential temperature, θ (a) and non-dimensional sensible heat flux $\langle w\theta \rangle \langle w\theta \rangle_0^{-1}$ (b) during the stable regime between 1400-1500 LST. Line types are as follows: criteria (a) (– –), criteria (b) (– · –), criteria (c) (– · –), 192^3 (——). 53

A.4 CComparison of LES total horizontal variances $\sigma_h w_*^{-1}$ (a) and vertical variance $\sigma_w w_*^{-1}$ (b) during the convective regime between 1500-1600 LST. Line types are as follows: criteria (a) (– –), criteria (b) (– · –), criteria (c) (– · –), 192^3 (——). 54

A.5 Comparisons of the LES time series for the stable regime of boundary layer height, H (a), surface sensible heat flux, $\langle w\theta \rangle_0$ (b), surface friction velocity, u_* (c), Obukhov length, and near surface wind direction, α with corresponding Clarke data $C71_0$. Line types are as follows: criteria (a) (– –), criteria (b) (– · –), criteria (c) (– · –), 192^3 (——). H81(▪), $C71_0$(•). 56

A.6 Comparison of LES potential temperature, θ (a) and sensible heat flux $\langle w\theta \rangle$ (b) during the stable regime between 2300-2400 LST. Line types are as follows: criteria (a) (– –), criteria (b) (– · –), criteria (c) (– · –), 192^3 (——). 57

LIST OF TABLES

3.1 Computational parameters and performance statistics 17
A.1 Details of AMR monitor functions from Eq. (3.18) for comparison study 51

ACKNOWLEDGMENTS

I would like to thank my wife, who lovingly supported me through the process of completing this work. Thank you to my parents, family, and everyone who has helped and supported me. I also thank my advisor who was a superb help in this research and Nathan Miller for the help through the years. Finally, I thank God for the merciful support.

CHAPTER 1

INTRODUCTION

The diurnal cycle of the atmospheric boundary layer (ABL) plays a critical role in many important physical, biological, and chemical processes. Understanding the transport of momentum, heat, water vapor, and pollutants is fundamental towards modeling these processes. In the ABL, the diurnal evolution of turbulence determines the nature of transport. During the day, incoming solar radiation heats the land surface causing strong positive sensible and latent heat fluxes that result in vigorous turbulent mixing. As a consequence of this mixing, the daytime convective boundary layer (CBL) is characterized by a deep boundary layer dominated by large coherent structures [5, 96]. At night, surface cooling suppresses mixing resulting in a shallow stable boundary layer (SBL) composed of localized turbulence [5, 96]. The wide range of length and time scales involved in these two regimes makes the ABL diurnal cycle a difficult topic to address.

The diurnal cycle has been studied experimentally and numerically. Experiments provide valuable statistics and characteristics describing the diurnal cycle [28, 78, 48, 8], but they provide limited information about the three-dimensional structure and unsteady behavior of turbulence. Alternatively, numerical simulations can provide three-dimensional, unsteady information about turbulent transport. Large-eddy simulation (LES) in particular has become a popular choice to model the distinct turbulent regimes of the diurnal cycle. Many of these studies have focused on the CBL (e.g., [31, 32, 69, 64, 100, 84, 75, 54, 62, 97, 98]). These studies have established that even relatively coarse resolutions can achieve expected results for first-order statistics. The low sensitivity of first-order statistics to grid resolution is usually attributed to the large fraction of resolved turbulent motions in CBL LES. Recently, Sullivan and Patton [98] determined that second- and third-order statistics are more sensitive to grid resolution. LES has also been used to study the SBL (e.g., [66, 20, 3, 57, 82, 14, 53, 15, 11, 95]). These studies have found that the SBL requires much finer grid resolutions for acceptable results. Beare et al. [15] concluded that a minimum resolution of 12.5 m in all directions was needed to sustain resolved turbulence in a weakly

stratified SBL, and that higher resolutions are required for statistics to become independent of grid resolution.

The difference in grid resolution requirements between the CBL and SBL becomes problematic when the entire diurnal cycle is simulated with one computational domain. The CBL height over homogenous terrain can be on the order of 2 km [85], demanding a large domain. The SBL requires finer resolution but for a much smaller domain of 250 m or less [57]. On a static grid, the contrast between these two regimes creates one of two problems for LES: either a fine resolution sufficient for the SBL on a domain large enough to model the daytime CBL must be used, or if an economical grid is chosen to match the extent and resolution requirements of the CBL, the SBL is under resolved. To avoid these problems, many researchers have focused on simulating only one particular regime and transition at a time, e.g., the CBL and evening decay [74, 87, 19, 44, 77, 13, 43, 80] and the morning transition [88, 12, 8]. The studies that have modeled the entire diurnal cycle with LES have used economical grids for the CBL period resulting in poor resolution of SBL processes.

Kumar et al. [59] simulated a diurnal cycle derived from the Horizontal Array Turbulence Study (HATS) data [48, 56]. They showed that LES could produce CBL growth and evolution, the formation of a nocturnal low-level jet (LLJ), and a recovery from stratified turbulence to a new CBL. However, they employed one-way surface forcing from prescribed fluxes, limiting the ability of the simulation to achieve realistic atmospheric stabilities in moderate to strongly stable situations [9]. Basu et al. [10] simulated 24 hours of the Wangara case [28] with LES using prescribed near surface air temperatures. They found that the simulations compared well to first-order experimental data and had expected total flux and variance statistics for both the convective and stable regimes. Moderate resolution results revealed a heavy reliance on the subgrid scale (SGS) model during the night. Caldwell and Bretherton [24] used LES to simulate the diurnal cycle to study boundary layer evolution and entrainment properties. They used a stretched determined *a priori* to focus on near surface and entrainment regions. Catalano and Cenedese [25] simulated the diurnal cycle in the presence of a valley. They used a stretched grid to increase resolution in the valley, where a cold pool formed at night with highly stable conditions. They found that nocturnal strongly stably conditions create dynamics that are difficult for LES to properly resolve. Recently, Kumar et al. [60] simulated a diurnal cycle based on the Cooperative Atmosphere-Surface Exchange Study–1999 (CASES-99) field campaign [78, 99]. Resolution sensitivity was not examined but the simulations did exhibit sensitivity to the type of

specification for both geostrophic winds and surface conditions. Specifically, prescribed surface fluxes had poorer performance than prescribed near surface air temperatures when compared against the experimental data.

These LES studies of the diurnal cycle relied on the quality of their SGS models to achieve acceptable results. Here, an alternative strategy is proposed that can be used in combination with any SGS model to improve the representation of the diurnal cycle with LES. Specifically, vertical adaptive mesh refinement (AMR) is employed in an attempt to better resolve the SBL and provide computational fidelity during all regimes, while maintaining computational affordability. AMR is a tool used in many computational fluid dynamic applications, ranging from engineering flows to large-scale atmospheric models. However, AMR has seen very little use in LES of the ABL and has never been used in combination with LES to model the diurnal cycle. This paper demonstrates the benefits and obstacles of combining LES and vertical AMR in simulations of a diurnal cycle.

The outline of this paper is organized as follows. First, an overview of AMR is presented with relevant techniques and applications to LES and the ABL. This is followed by the methods and numerical procedures of the current study, along with the details of the simulated case based on days 33 to 34 of the Wangara experiment [28]. Next, the results and findings of LES with vertical AMR compared against LES with static grids are detailed, and then conclusions and future directions are given.

CHAPTER 2

ADAPTIVE MESH REFINEMENT

In 1966 Charney [26] envisioned a new type of numeric solver which would allow "the computational lattice itself to distort as the flow evolves in such a way that the lattice spacing adjusts to the gradient of the quantity one wishes to resolve" [35]. Actual implementation of AMR has roots back to 1975 from the research of Babuska [6] who coined the term self-adaptation [16]. Today AMR has evolved into having two main components: a method of adapting the grid and a criteria to govern adaptation, known as a monitor function.

There are three basic categories of AMR methods: p-refinement, h-refinement, and r-refinement [40, 16, 49]. In p-refinement the computational numerics used to solve a set of governing equations are dynamically increased or decreased in order of accuracy, as determined by the monitor function, and the mesh spacing is held fixed. The drawbacks of this method include increased code complexity with increasing numerical accuracy and the fact that a numerical method with a higher order of accuracy does not always guarantee improved results [61]. In h-refinement, the number of nodes is variable and nodes are added, subtracted, and reorganized based on the monitor function. Therefore, the simulation cost can grow or shrink and the quality and shape of the mesh can be readily controlled. However, this method can be costly with the addition of too many points and grid architecture can become distorted [108]. In r-refinement, the number of computational grid points stays constant and are instead rearranged by the monitor function. Mesh size and accuracy can be efficiently used for a set computational cost. Still, the method can be costly when used in many dimensions and the computational elements can become distorted, move too fast or too far, or cause areas to be devoid of nodes [102].

The monitor function is typically formed with either one or a combination of characteristic criteria. These criteria are used to locate areas of high physical or numerical significance. Typically these include regions of high gradients, i.e., vorticity, shock, near interfaces, etc. Other regions of interest can also be targeted, such as high pollutant concentrations or

truncation error [21]. Once located, the monitor function allocates nodes or increases numerics in these areas to provide increased resolution and computational accuracy. In LES in particular, the use of AMR can not only improve numerical accuracy, but reduce the dependence on the SGS model with increased resolution [81]. In the end, choosing a suitable criteria is one of the most challenging, subjective, and important concepts of AMR [63]. For more detailed information on the AMR techniques and criteria selection, refer to Thompson [102], Hawken et al. [45], Garg [40], and Huang and Russell [49].

2.1 AMR combined with LES in general

AMR with LES has been used in small scale applications with acceptable results, however the techniques are still in development. Early work combining AMR with LES focused on grid nesting [29, 67]. This type of AMR built on the efforts of Berger and Oliger [17], who pioneered nested grid AMR methods. Cook [29] kept uniform spacing at each nested grid level in order to keep filter width constant and avoid commutation errors from varying filter widths. He concluded that commutation errors between nested grids are present but remain small and localized. Mitran [67] found that AMR on a structured grid performed better than AMR on an unstructured grid. The AMR monitor function criteria was based on the combination of both truncation error and physical indicators used to pinpoint areas deviating from near-isotropic turbulence. It was found that solitary use of one of these criteria provided undesirable refinement (a common problem with selecting an AMR criteria). In a similar type of method to LES, Goldstein and Vasilyev [42] proposed stochastic coherent adaptive large-eddy simulation (SCALES) solve multi-scale flow dynamics. SCALES uses wavelet methods to "track" coherent energetic eddies and to better resolve them to improve the energy resolution of the simulation.

Naudin et al. [72] evaluated the use of h-refinement AMR with the simulation of a swirl burner. They found that the use of AMR in LES could provide a simulation of equal quality to one of fifteen times the computational cost. The premise of their refinement was to find the optimal balance between SGS and total turbulent kinetic energy. Pantano et al. [76] combined LES with nested grids and successfully simulated turbulent jet and shock problems. They found that nested grid interfaces must be handled carefully to prevent artificial energy gain/loss. More recently, Aristodemou et al. [4] used LES with AMR to simulate airflow in an urban landscape scaled down to wind tunnel size. The h-refinement method was based on minimizing the error in the numerical representation of the velocity gradients and setting upper and lower bounds on the grid spacings. Simulated

wind and turbulent fluctuations generally matched wind tunnel data of the experimental setup, especially with simulations that were set to achieve finer resolutions. A substantial gain in efficiency resulted from the AMR applications.

2.2 AMR used in ABL simulations

To the author's knowledge, ABL simulations using AMR with LES have not been performed previously. The closest example is the work of Stevens and Bretherton [92] who implemented moving refined nested grids in stratocumulus cloud simulations. Grid movement was chosen *a priori* to follow the cloud region and did not include any feedback from the velocity or scalar fields. Good approximations were obtained at a computational time and storage cost of 25 percent of a fine static grid. Alternatively, static grids that are stretched and refined *a priori* have been a popular choice to obtain desired grid resolutions. The cloud modeling community have employed many nested and stretched grids to cluster points in the boundary layer and around the entrainment zone (e.g., [97, 91, 24, 27, 104]). Momentum and scalar transport during the morning transition was analyzed by Beare [12] who used a stretched grid ranging from 5-20 m. Their method was also complicated by using *a priori* domain expansions as the CBL formed and grew beyond the extent of the original domain requiring sub-grid model alterations. Others have tried to determine the best grid distribution *a priori* with more deterministic approaches. Degrazia et al. [34] took into account the turbulence inhomogeneity of the CBL and derived a formula for a static stretched grid for use in LES. An initial RANS model of a simulation case was run by Zhang et al. [107] to get flow statistics to use as criteria to design a grid. Others [58, 101] have done work using statically refined grids with LES to further this genre of mesh generation.

Atmospheric research efforts other than LES have been using AMR to improve their simulations for some time. For example, Dietachmayer and Droegemeier [35] and Fiedler and Trapp [39] implemented the continuous dynamic grid adaption (CDGA) r-refinement method (pioneered by Brackbill and Saltzman [18]) to analyze two- and three-dimensional rising thermals. Dietachmayer and Droegemeier [35] used monitor function criteria based on numerical errors and first and second velocity gradients. Skamarock and Klemp [86] applied dynamic nested grids with a truncation error criteria to solve atmospheric flow equations on mesoscale domains, while Almgren et al. [2] modeled the release of a hot gas in the atmosphere with an hierarchy of grids. Other approaches have also been taken including the development of the operational mulitscale environmental model with grid adaptivity (OMEGA) by Bacon et al. [7]. OMEGA is an unstructured grid RANS solver that uses an

h-refinement adaption technique.

Much of the prior utilization of AMR for atmospheric simulations has been used to model pollutant and other scalar transports in mesoscale models. Tomlin et al. [103] and Srivastava et al. [89] successfully modeled two-dimensional mesoscale atmospheric emissions to study pollutant transport. h-refinement and r-refinement were used respectively based on concentration characteristics. Later, Iselin et al. [52, 51] used dynamic grid adaption (DGA) in unison with the advection equation solver MPDATA (multidimensional positive definite advection transport algorithm) for two- and three-dimensional simulations. Grid adaptation was only performed in horizontal dimensions on block structured grids, keeping wall-normal grid columns in line. Both accuracy and efficiency benefits were observed. Hubbard and Nikiforakis [50] developed a global model to solve the scalar transport equations incorporating the nested AMR method [17]. For a more complete review of the use of AMR for mesoscale applications see Iselin et al. [52, 51], Schimmel [83], and Behrens [16].

On an ABL scale with vertical AMR, Fiedler [38] used a single-column model (SCM) to analyze entrainment rates within smoke and water clouds. r-refinement grid adaption functionals were derived from the ABL height and tunable parameters. The model produced improved results over static grid models, but did not provide significant improvements to overcome the deficiency of the base numerical model. Dunbar et al. [36] used a similar SCM with AMR to simulate the stable case of Cuxart et al. [30] and diurnal cycle case of Svensson et al. [99]. They used a monitor function based on the first and second gradients of potential temperature to drive an r-refinement method through the equidistribution technique (explained in section 3.2). In comparison to high resolution static simulations, including AMR resulted in simulations with less error than simulations of the same number of equally spaced nodes . The AMR simulations also successfully qualitatively modeled the diurnal cycle producing expected trends in velocity, potential temperature and turbulent kinetic energy profiles. Marchand and Ackerman [63] added vertical layers into the System for Atmospheric Modeling (SAM) two-dimensional cloud resolving model. Refinement designation was based on the change in domain averaged potential temperature profile, estimated SGS to total water flux, and SGS to total turbulent kinetic energy. The results were similar to that of higher resolution, equally spaced simulations with much less computational overhead.

CHAPTER 3

NUMERICAL SIMULATION

3.1 LES methods

The framework of the LES code used in this study follows Stoll and Porté-Agel [93, 95] with modifications to accommodate AMR. The code solves the filtered incompressible Navier-Stokes and continuity equations

$$\frac{\partial \widetilde{u_i}}{\partial t} + \frac{\partial \widetilde{u_i}\widetilde{u_j}}{\partial x_j} = -\delta_{i3} g \frac{\widetilde{\theta_v} - \left\langle \widetilde{\theta_v} \right\rangle}{\theta_{v,0}} - \frac{\partial \widetilde{p^*}}{\partial x_i} - \varepsilon_{ij3} f_c \left(U_{g,j} - \widetilde{u_j} \right) - \frac{\partial \tau_{ij}}{\partial x_j} \tag{3.1}$$

and

$$\frac{\partial \widetilde{u_j}}{\partial x_j} = 0, \tag{3.2}$$

along with the filtered scalar concentration equations for both temperature

$$\frac{\partial \tilde{\theta}}{\partial t} + \tilde{u}_j \frac{\partial \tilde{\theta}}{\partial x_j} = -\frac{\partial \pi_{\theta,i}}{\partial x_j} \tag{3.3}$$

and humidity

$$\frac{\partial \tilde{q}}{\partial t} + \tilde{u}_j \frac{\partial \tilde{q}}{\partial x_j} = -\frac{\partial \pi_{q,i}}{\partial x_j}. \tag{3.4}$$

In Eq. (3.1-3.4), the tilde denotes the LES low-pass filtering operation at scale Δ_f, with $\Delta_f \geqslant \Delta_g$, where Δ_g denotes the grid spacing, and $\langle\rangle$ denotes a horizontal average. The subscripts i, j, and k correspond to the streamwise (x), spanwise (y) and vertical (z) directions. u_i is the velocity in the i-direction, x_i is the spacial position in the i-direction, t is time, $\widetilde{p^*} = \tilde{p} + \frac{1}{2}\widetilde{u_i}\widetilde{u_i}$ is the filtered dynamic pressure, τ_{ij} is SGS scalar flux, δ_{ij} is the Kronecker delta function, $\widetilde{\theta_v}$ is the filtered virtual potential temperature, g is gravitational acceleration, f_c is the Coriolis parameter, ε_{ijk} is the alternating unit tensor, $\tilde{\theta}$ and $\tilde{q}$ are the filtered scalar concentration of potential temperature and specific humidity respectively, and $\pi_{\theta,i}$ and $\pi_{q,i}$ are the scalar SGS flux terms. Inherent in Eqs. (3.1), (3.3), and (3.4) are some important assumptions. Viscous dissipation and molecular diffusion have been neglected due to their relatively small magnitude in the ABL compared to the other terms

in Eqs. (3.1), (3.3), and (3.4), the Boussinesq approximation is used to account for buoyancy effects, and the definition of the geostrophic wind is used to replace mean horizontal pressure gradients [96].

LES results been found to be sensitive to the formulation of the SGS terms, τ_{ij} and $q_{C,i}$, especially in the SBL [15, 95, 8]. In this research the scale-dependent Lagrangian dynamic model, developed by Stoll and Porté-Agel [94] is utilized. This model has been validated in a wide variety of ABL conditions [94, 95].

Eq. (3.1), (3.3), and (3.4) were advanced in time with a second-order Adams-Bashforth scheme. Pseudo-spectral methods were employed in horizontal space. Finite difference methods were used to perform vertical calculations. In Stoll and Porté-Agel [93, 95], vertical derivatives were approximated with second-order central finite difference schemes evaluated on equally spaced computational nodes. In this study both the first and second derivatives have been modified to use second-order polynomial fitting resulting in the following second-order accurate first derivative [37]:

$$\left(\frac{\partial \phi}{\partial z}\right)_m = \frac{\phi_{m+1}(\Delta z_m)^2 - \phi_{m-1}(\Delta z_{m+1})^2 + \phi_m[(\Delta z{+}1)^2 - (\Delta z_m)^2]}{\Delta z_{m+1}\Delta z_m(\Delta z_m + \Delta z_{m+1})} \tag{3.5}$$

where ϕ_m is any variable at node m and grid spacings are defined as $\Delta z_m = z_m - z_{m-1}$ and $\Delta z_{m+1} = z_{m+1} - z_m$. The code uses a staggered grid with vertical velocity information stored on nodes starting at $z = 0$, while u,v,p,θ, and q information are stored on nodes (u-nodes) that lie equidistant between w-nodes. Since ϕ_m in Eq. (3.5) is not explicitly stored, interpolation was used to provide the approximation necessary to evaluate the derivative.

Continuity is satisfied through the solution of a Poisson equation for pressure that results from taking the divergence of Eq. (3.1) and applying the conservation of mass. Second derivatives required for this calculation were performed by evaluating first derivatives as explained above, followed by taking the first derivative of the first derivatives. This process was used in order to maintain numerical consistency, which Albertson [1] cautions is essential for the pressure field to remove any pre-existing velocity divergence.

3.2 AMR method

r-refinement was selected to provide the AMR for these simulations. Both h-refinement and r-refinement would be applicable for a one-dimensional AMR with LES of the ABL and would likely behave very similarly in this application. While h-refinement has the benefit of supplying the optimal resolution everywhere for LES by adding and subtracting points as necessary, it is not anticipated that the total number of grid points will decrease in ABL

simulations. Studies of both the CBL [98] and the SBL [8] have shown that even extremely high resolutions have yet to achieve results that are completely independent of the grid spacing. Therefore, r-refinement was chosen to use the available number of grid points, i.e., computation resources, as efficiently as possible.

The equidistribution principle was employed as the mechanism to perform the r-refinement. In any one dimension, the equidistribution principle states that grid points must be positioned in order to equally distribute some positive weight function between each pair of nodes [41]. This is expressed mathematically as:

$$\int_{z_m-1}^{z_m} \Omega(z)dz = constant, \tag{3.6}$$

or discretely

$$\Omega_m \Delta z_m = constant, \tag{3.7}$$

where Ω_m is a weight function, derived from the monitor function. Ω_m is assumed constant across any individual grid spacing. This system of equations is often related to a system of springs, where Δz_m is the spring length and Ω_m represents the spring stiffness. In this analogy, directly related to Hooke's law [49], each spring is connected at each of its two points m and $m-1$ to either another spring or a stationary wall (in the case of the top and bottom springs). Larger values of the weight function act as stiff springs and lower values are correspondingly weak springs. Eq. (3.6) can be solved to bring the system into equilibrium, by contracting Δz_m in areas of high Ω_m and expanding Δz_m in areas of low Ω_m. By distributing the "spring force", $\Omega_m \Delta z_m$, across all points, the total weight function is minimized globally across the system. [71]

Procedurally, an iterative scheme is used to solve the system of equations represented by Eq. (3.7) [102]. This process begins by assigning weight function values for each grid spacing on the original grid and subsequently solving Eq. (3.7) to bring the system of springs into equilibrium. Following an iteration, the grid points are relocated and hence lie in areas where the original weight function, obtained from the monitor function of the flow field at the original points, may have different values. Values of the weight function are interpolated to the new spring spacings and the process is repeated. When the system has converged the process is halted.

If Eq. (3.7) is simply solved, the minimum and maximum grid spacings will be based solely on the monitor function, potentially resulting in very large and small grid cells with anisotropic shapes. In LES, various restrictions are placed on the code that affect the selection of minimum and maximum grid spacings. The subgrid model makes assumptions

of isotropy that should be adhered to so that the model is valid. RANS models are inherently less sensitive to grid resolution and aspect ratios allowing Fiedler [38] and Dunbar et al. [36] to use Eq. (3.7) with less concern about the minimum and maximum grid spacings. In LES, a more robust method is required to prevent instability and limit grid anisotropy.

Nakahashi and Deiwert [70, 71] developed a method of equidistribution that overcame the empiricism of selecting monitor functions that provided desirable maximum and minimum grid spacings. This method requires the minimum and maximum grid spacings to be specified beforehand, and then solves the equidistribution equation *as best as possible* with these spacing restrictions. This method does compromise a perfect equidistribution of the monitor function. However, the monitor functions primary goal is to arrange the grid points to achieve increased resolution in areas of interest [52], therefore this approach is appropriate [41] accomplishing the intent of the scheme *as best as possible*.

3.2.1 AMR numerics

The following is the set of equations and processes derived by Nakahashi and Deiwert [71] used in this study (also found in Garg [40]). Any grid spacing, Δz_m, between two points z_m and z_{m-1}, for any N number of grid points comprising an overall length L_g, can be calculated from an evaluation of Eq. (3.6) as

$$\Delta z_m = \frac{L_g}{\Omega_m \sum_{n=1}^{N} \frac{1}{\Omega_n}}. \tag{3.8}$$

The weight function, Ω_m, is assigned as

$$\Omega_m = 1 + A\overline{f}^B, \quad \text{where} \quad \overline{f} = \frac{f_m - f_{min}}{f_{max} - f_{min}}. \tag{3.9}$$

Here f_m is the monitor function defined by solution errors and/or parameters. Variables A and B are positive constants and are determined with the following process. A is assigned

$$A = \frac{\Delta z_{max}}{\Delta z_{min}} - 1, \tag{3.10}$$

and B is found by

$$B^{s+1} = B^s + \Delta B^s, \tag{3.11}$$

where

$$\Delta B^s = \left[\Delta z_{min} - \min\left(\Delta z_m\right)^s\right] / \left[\frac{\partial \min\left(\Delta z_m\right)}{\partial B}\right] \tag{3.12}$$

and

$$\frac{\partial \min\left(\Delta z_m\right)}{\partial B} = -A \sum_{n=1}^{N} \left[\Delta z_m \left(\frac{\delta_{mn}}{\Omega_m} - \frac{\Omega_m}{\Omega_n^2}\frac{\Delta z_m}{L_g}\right) \overline{f}_n^B \log \overline{f}_n\right]. \tag{3.13}$$

Eq. (3.8)-(3.13) are iteratively repeated until convergence is achieved. Convergence is deemed satisfied when the weight function has been best distributed throughout the domain amongst the grid spacings to some set criteria.

Procedurally, in order to properly move the grid points, the grid movement must be accounted for in the conservation equations with an additional grid velocity in the advection term. [23, 22, 47, 38, 36]. This velocity, w_g, is defined as

$$w_g = \frac{\partial z}{\partial t}, \tag{3.14}$$

and is removed from the vertical velocity, $\tilde{w}$ in the advection terms of equations (3.1), (3.3), and (3.4). Hence the advection terms become respectively:

$$\frac{\partial \widetilde{u}_i \widetilde{u}_j}{\partial x_j} => \frac{\partial \widetilde{u}_i (\widetilde{u}_j + \delta_{j3} w_g)}{\partial x_j}, \tag{3.15}$$

$$\tilde{u}_j \frac{\partial \tilde{\theta}}{\partial x_j} => (\tilde{u}_j + \delta_{j3} w_g) \frac{\partial \tilde{\theta}}{\partial x_j}, \tag{3.16}$$

and

$$\tilde{u}_j \frac{\partial \tilde{q}}{\partial x_j} => (\tilde{u}_j + \delta_{j3} w_g) \frac{\partial \tilde{q}}{\partial x_j}. \tag{3.17}$$

In this work, grid movement was not performed every step (as did Aristodemou et al [4]), but rather every 50 time steps. More frequent grid updating was tested and caused little change in grid spacing over short periods of time and subsequently little change in the simulation results.

3.2.2 Monitor function

Multiple criteria were tried in the monitor function. Namely, the vertical gradient of the mean wind, the vertical gradient of potential temperature, and vertical potential temperature profile were all tested either alone or in combination with one another. The normalized combination of all three was found to be the most stable and suitable to provide grid clustering where needed in the simulation domain. The combined monitor function is defined for any height m as:

$$f_m = \lambda_1 \frac{\frac{d\langle M_m \rangle}{dz_m}}{\left(\frac{d\langle M \rangle}{dz}\right)_{max}} + \lambda_2 \frac{\frac{d\langle \theta_m \rangle}{dz_m}}{\left(\frac{d\langle \theta \rangle}{dz}\right)_{max}} + \lambda_3 \frac{\langle \theta \rangle_{max} - \langle \theta_m \rangle}{(\langle \theta \rangle_{max} - \langle \theta_m \rangle)_{max}}. \tag{3.18}$$

Here the first term serves to cluster grid points in areas of high velocity shear. The second term focuses grid points in areas of high vertical potential temperature gradient. The last term serves as a "mapping" by utilizing the ABL potential temperature profile and adiabatic lapse rate to prevent clustering in the sponge and residual layers. The adiabatic lapse rate

above the ABL has a near linear increase in temperature starting at the top of the CBL up to the warmest point at the top of the domain. By comparing temperatures to this maximum, the cooler portion of the domain, i.e., the CBL and SBL, will have the largest weight values keeping points in the boundary layers. λ_1, λ_2, and λ_3 are weighting constants chosen ad hoc to place emphasis on certain aspects of the flow. For a comparison of results from the different criteria and to see the effect of the different terms in this monitor function, see the appendix.

3.3 Case description

The Wangara case study provides a challenging test bed for LES of the diurnal cycle of the ABL and was also performed with LES by Deardorff [32, 33], Moeng [69], Xue et al. [105] and most recently Basu et al. [10]. Only Basu et al. [10] completed the full diurnal cycle while the others only simulated the daytime conditions. The experimental data was obtained by Clarke et al. [28] beginning on 16 August 1967 (day 33 of the entire Wangara experiment) at 0900 local standard time (LST) and ending on 0900 LST 17 August (day 34 of the experiment). The Wangara test site is located in western Australia at a location of $34^\circ 30' $ S., $144^\circ 30'$ E. The terrain of the site had only sparse vegetation on a flat area and the conditions were clear skies, very little horizontal advection of heat and moisture, and a lack of any frontal activity within 1000 km. This provided an "ideal" situation for testing boundary layer parameterizations [32, 10]. During the experiment, vertical measurements were taken for velocity, temperature, and moisture. Directions were oriented with positive x and u due east and positive y and v due north. Due to the dryness of the period, some studies have neglected the effect of moisture and still produced good simulations of this experiment [69, 90, 10]. In this study moisture is included, as did other successful studies [106, 79].

3.3.1 Initial conditions, boundary conditions, and forcings

Initial conditions for all three components of velocity, temperature, and specific humidity were generated from the soundings obtained by Clarke et al. [28] at 0900 LST on day 33. The physical domain size chosen for the simulations was 5 km $\times$ 5 km $\times$ 2 km high. Periodic horizontal boundary conditions were used. Surface conditions were prescribed by setting the vertical velocity to zero at the surface and the surface conditions of the remaining velocity, potential temperature, and moisture fields were calculated using Monin-Obukhov similarity theory. Although Monin-Obukhov similarity theory is formulated for steady flows, it will be used locally in this study for lack of a better alternative as has been done previously

(e.g., [93, 94, 95]). These surface condition equations are:

$$(w\theta)_0 = u_*\theta_* = \frac{\kappa u_*(\widetilde{\theta_1} - \theta_{(1.2)})}{\ln\left(\frac{z_1}{1.2}\right) + \Psi_H\left(\frac{z_1}{L}\right) - \Psi_H\left(\frac{1.2}{L}\right)}, \tag{3.19}$$

$$(wq)_0 = u_*q_* = \frac{\kappa u_*(\widetilde{q_1} - q_{(1.2)})}{\ln\left(\frac{z_1}{1.2}\right) + \Psi_H\left(\frac{z_1}{L}\right) - \Psi_H\left(\frac{1.2}{L}\right)}, \tag{3.20}$$

and

$$\sqrt{\tau_s} = u_* = \frac{\kappa\tilde{M}}{\ln\left(\frac{z_1}{z_0}\right) + \Psi_M\left(\frac{z_1}{L}\right) - \Psi_M\left(\frac{z_0}{L}\right)} \tag{3.21}$$

where $\kappa = 0.4$ is the von Karman constant, u_* is the surface friction velocity, θ_* and q_* are surface scalar scales, $\widetilde{\theta_1}$ and $\tilde{q}_1$ are the local, filtered, scalar values at the first u-node, z_1, and $\tilde{M}_1$ is the local, filtered, mean velocity at z_1. $\theta_{(1.2)}$ and $q_{(1.2)}$ are the scalar values measured at the screen height of 1.2 m. The time series of screen values, as shown in Fig. 3.1, were recorded every hour for temperature and every three hours for moisture by Clarke et al. [28] and linearly interpolated in time to provide values at each LES time step. The terrain of the Wangara site had only sparse vegetation on a flat area, leading to the surface roughness parameter $z_0 = 0.01$ m. Ψ_H and Ψ_M are empirical stability correction terms as a function of the Monin-Obukhov length, L, and are defined for the different atmospheric stability conditions by Arya [5].

Top boundary conditions were set as zero stress for momentum and an inversion strength of 0.001 K m^{-1} and 0 kg/kg for temperature and moisture respectively. A Rayleigh damping layer was initiated at 1500 m up to the top of the domain. Vertical profiles for geostrophic wind forcings were calculated following Yamada and Mellor [106] based on measured thermal wind and surface geostrophic wind data. Contour plots of the geostrophic winds are provided in Fig. 3.2. The Coriolis parameter was set to $f_c = -0.826 \times 10^{-4}$ s^{-1}.

3.4 Resolutions and simulations

In order to analyze the behavior of LES with AMR, a LES with vertical AMR was compared against static grid simulations of equal and higher resolutions. Table 3.1 provides a description of variable simulation parameters. The coarsest resolution of 96^3 grid points was run with both a static grid and one with AMR. These simulations were compared against the highest static resolution of 192^3 grid points. A time step of 0.4167 s was used for the 192^3 simulation with a doubled time step for the 96^3 static and AMR simulations. For the AMR simulation, the minimum grid spacing was chosen based on the work of Beare et al. [15], who found that 6.25 m spacing (in all directions) provided good results in a

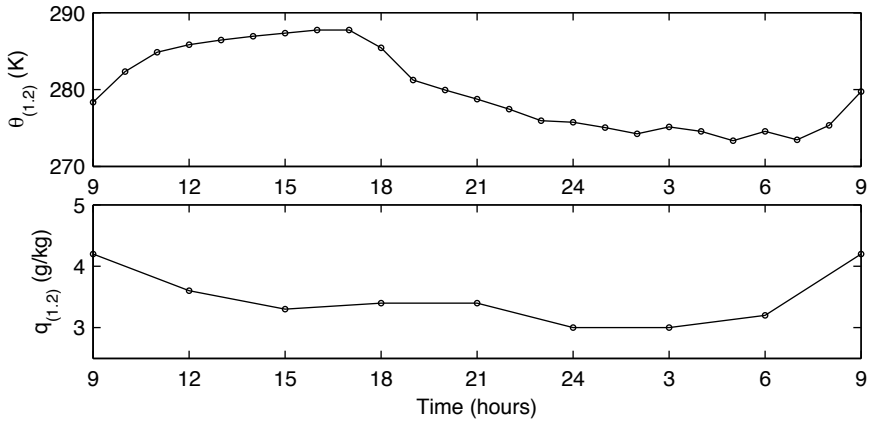

Figure 3.1. Time series of the potential temperature and moisture screen measurements [28].

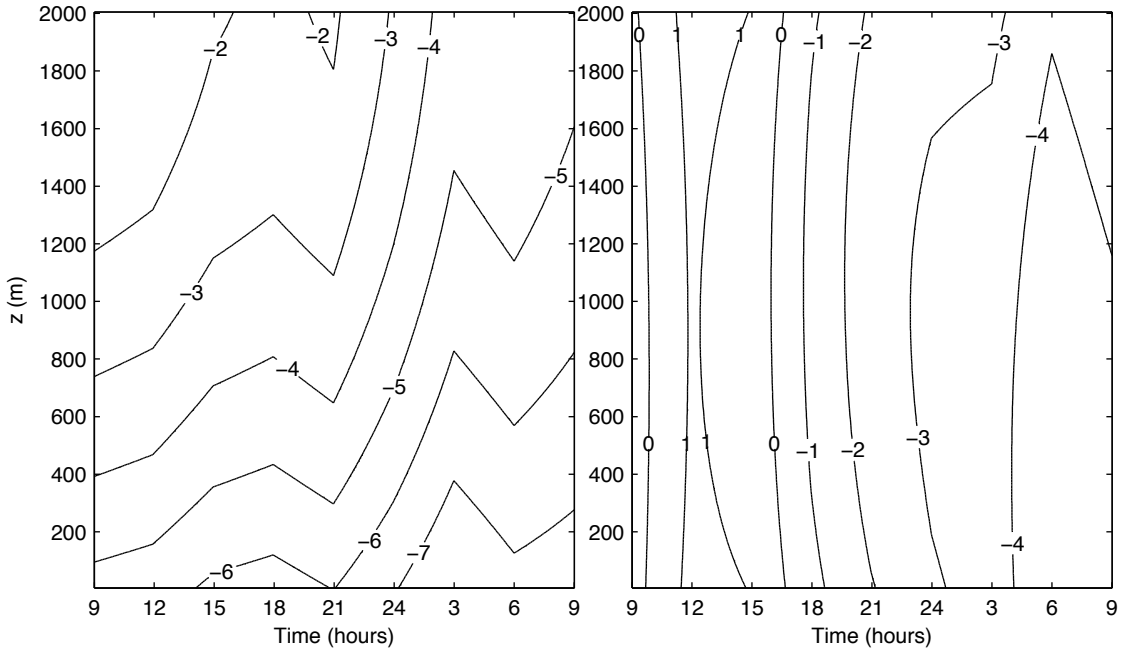

Figure 3.2. Time-height contours for geostrophic winds: streamwise (left) and spanwise (right) [106].

weak to moderate SBL. The maximum spacing was chosen to be large enough to facilitate a sufficient quantity of fine spacings and avoid grid cells that were taller than they were wide in the boundary layer. In addition, a simulation of $96 \times 96 \times 192$ grid points in the $x \times y \times z$ directions was used to distinguish between the effects of horizontal and vertical resolution. It will be displayed when necessary to support findings. An explicit filtering of $2 \times \Delta_g$ was used in each simulation.

3.4.1 Computational costs

The goal of AMR is to obtain the same statistical quality as higher resolution simulations at a reduced cost, thus improving both the quality of simulations (for a given available resource) and the efficiency. Table 3.1 also provides the computational overhead statistics. Even with the state of the art, massively parallel computational resources used (Center for High Performance Computing at the University of Utah) the 192^3 simulation is computationally burdensome for testing purposes. The 96^3 simulations are inexpensive and facilitate efficient hypothesis testing. As denoted in the table, the AMR was tested with implementation every 50 and 10 steps to analyze its cost. It was found that the cost of the AMR was negligible, and the difference in times between the 96^3 simulations is attributed to the load on the computing center. It is also noteworthy that the iterative scheme used to solve the grid equidistribution equations usually converged in less than ten iterations.

Table 3.1. Computational parameters and performance statistics

Simulation	$\Delta x, \Delta y$ (m)	Δz (m)	Processors	Time steps	Total Hours
192^3	26.04	10.47	192	207360	43.52
96^3	52.08	21.05	96	103680	4.98
96^3 AMR (50 steps)	52.08	6.25-30.00	96	103680	4.91
96^3 AMR (10 steps)	52.08	6.25-30.00	96	103680	4.93

CHAPTER 4

RESULTS AND DISCUSSIONS

In this section simulation results for the Wangara day 33-34 diurnal case are presented for both static and vertical AMR grids. The focus is on the performance of the AMR simulations with respect to the uniformly spaced, static grid simulations. During the simulations, statistics were sampled every five minutes of physical time and averaged over horizontal planes. Fluctuations needed to calculate turbulent fluxes where calculated as deviations from the horizontal plane averaged values. Both hourly averages and instantaneous five minute profiles of the horizontally averaged variables are presented. Simulation results are presented in three sections. First, the high resolution simulation results are compared to the experimental data of Clarke et al. [28] to establish the ability of the LES numerical code to reproduce the basic features of the diurnal cycle. Next, the diurnal cycle is broken up into a convective regime (1100 LST to 1630 LST on day 33) and a stable regime (2000 LST on day 33 to 0600 LST on day 34). This separation of stability regimes is chosen to facilitate detailed analysis of the ability of vertical AMR simulations to reproduce high resolution results at a greatly reduced computational cost with a single computational grid. Although the evening and morning transition periods are critical components of the diurnal cycle [12, 80], they are not examined in detail in this study.

4.1 Comparison to Wangara data

The first step in examining the ability of vertical AMR to efficiently reproduce high resolution, diurnal cycle simulation results at a reduced cost is to establish the ability of the LES to reproduce a physically realistic diurnal cycle. To accomplish this, mean velocity and potential temperature profiles from the high resolution simulation are compared to the experimental data of Clarke et al. [28]. Fig. 4.1 compares the mean wind and potential temperature profiles for the entire diurnal cycle. During the day in the CBL, both the experimental and LES results have wind speeds that are relatively constant with height with increasing mean wind speeds throughout the evening and into the night. During the

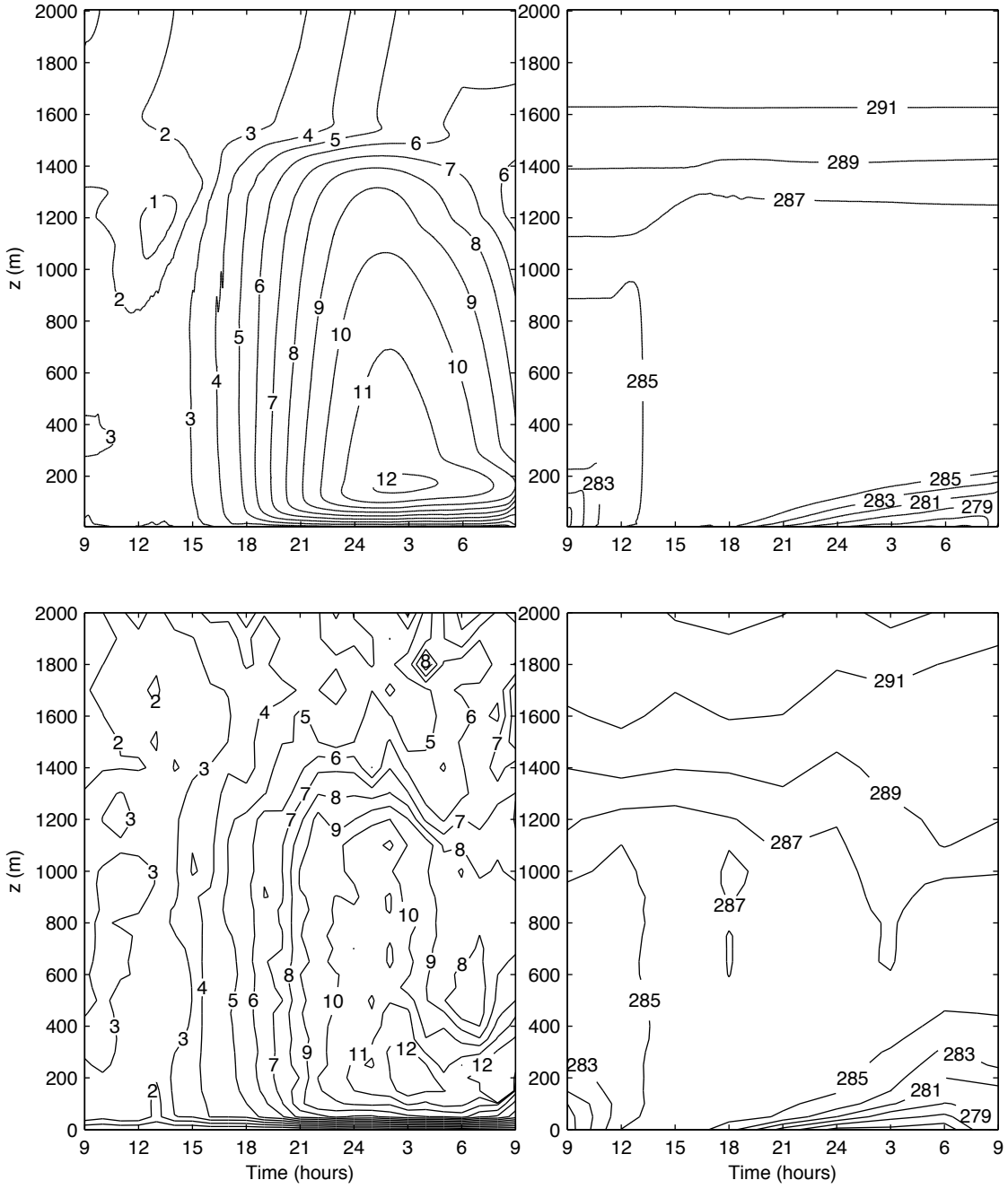

Figure 4.1. Time-height contours for LES 192^3 results (top) versus Wangara data (bottom) for mean wind speed (left) and potential temperature (right).

nocturnal hours of the experimental and LES results, a low-level jet (LLJ) forms around 0000 LST and lasts into the early morning of day 34. The LES potential temperature contours during the day, between 0900-1600 LST on day 33, compare well to the experimental data portraying the well mixed boundary layer. At night, before 0000 LST the LES and experimental data still compare well but the LES underestimates the temperature with height in the boundary layer. Through the night and during the early morning hours, the simulation results switch to overestimate the potential temperature profile with height.

Figs. 4.2 and 4.3 give instantaneous vertical profiles for a more detailed comparison of the convective and stable regimes, respectively. In Fig. 4.2, the LES underestimates the mean velocity in the early hours of the convective regime compared to the experimental data. This behavior is attributed to be a direct result of the initial conditions. As time advances and the CBL height grows with increased mixing, the agreement between the experimental data and the simulated velocity profiles improves. Additionally, potential temperature profiles compare well during the day as described above. During the stable period, given in Fig. 4.3, the main difference in velocity can be seen in the magnitude of the LLJ. The LES results underestimate the magnitude, height and vertical spread of the jet peak. Potential temperature profiles match well in the lower portion of the SBL for all nocturnal hours. However, starting at 0000 LST the LES results have a more abrupt transition into the residual layer at a location closer to the ground. This results in a potential temperature that is warmer with height for the LES results starting at the bottom of the residual layer. The differences between the experimental data and LES results widen as the night advances and the experimental results become cooler with height. Similar results for velocity and potential temperature have been observed by other Wangara days 33-34 studies (e.g., [106, 55, 10]).

Fig. 4.4 shows the characteristic time series for the case. Included are boundary layer height (BLH), surface sensible heat flux, surface friction velocity, Obukhov length and wind direction (α) measured from positive x (due east) at z_1 and approximately 100 m. The CBL height, z_i, is measured as the location of the minimum sensible heat flux and the SBL height, H, is estimated as the location at which the mean shear stress falls to ten percent of the surface value. The CBL has a maximum height of approximately 1400 m just before 1800 LST. During the night the SBL height begins below 75 m at 1900 LST and grows steadily throughout the night to about 180 m. Included along with the flux and stability results are data points calculated by Hicks [46]. Compared to the data of Hicks [46], the LES daytime surface sensible heat flux is underestimated by nearly 100 percent, and the LES nighttime

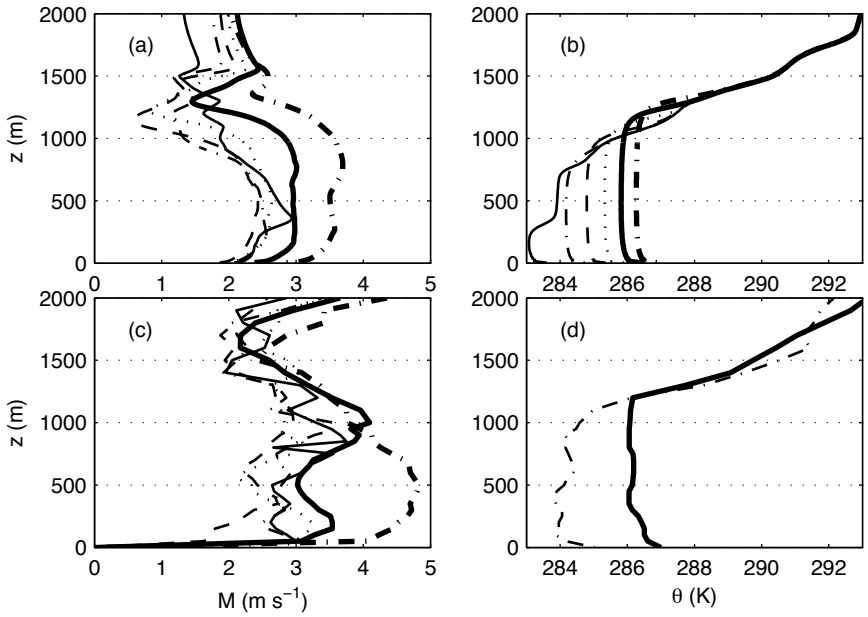

Figure 4.2. Comparison of plane averaged, instantaneous vertical profiles for LES 192^3 (a,b) versus instantaneous Wangara data (c,d). Mean wind speed (a,c) and potential temperature (b,d) are provided for the convective regime. Line types are as follows: 1100 LST (——), 1200 LST (– · –), 1300 LST (– –), 1400 LST (· · · · ·), 1500 LST (▬▬), 1600 LST (▬ · ▬).

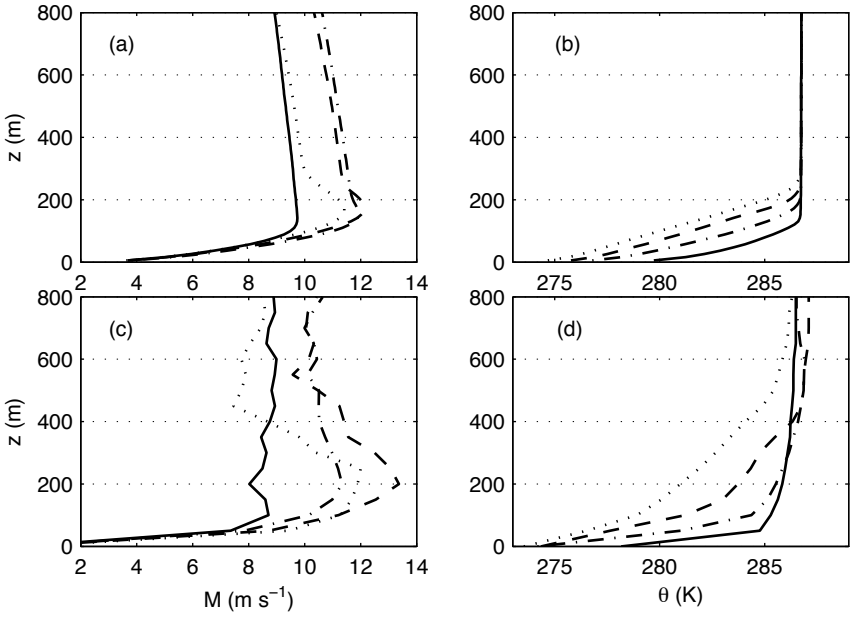

Figure 4.3. Comparison of plane averaged, instantaneous vertical profiles for LES 192^3 (a,b) versus instantaneous Wangara data (c,d). Mean wind speed (a,c) and potential temperature (b,d) are provided for the stable regime. Line types are as follows: 2100 LST (——), 0000 LST (– · –), 0300 LST (– –),0600 LST (· · · · ·)

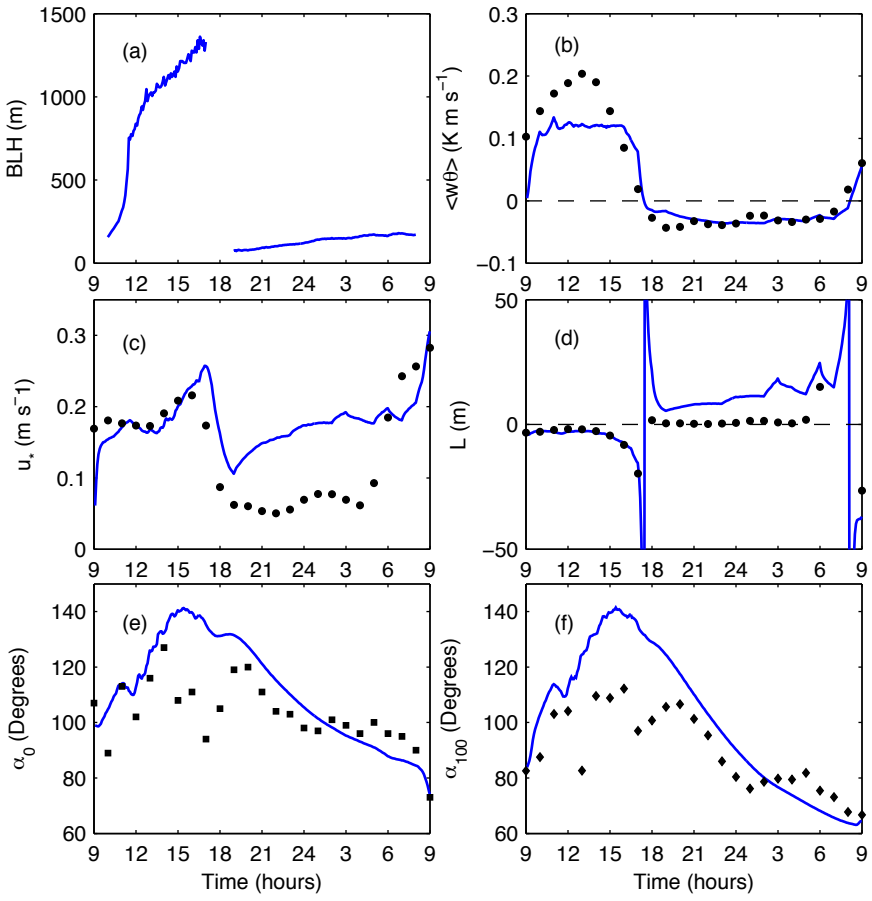

Figure 4.4. Time series obtained from 192^3 LES. boundary layer height, BLH (a), surface sensible heat flux, $\langle w\theta \rangle_0$ (b), surface friction velocity, u_* (c), Obukhov length, L (d), wind direction near the ground, α_0 (e), and wind direction at approximately 100 m, α_{100} (f)

surface sensible heat flux closely matches the data. During the day, u_* is predicted well up to the transition, however there is a lag in the transition followed by a drastic over estimation at night. This indicates that the LES surface flux dependence on momentum forcings is too strong, that the momentum forcing is specified incorrectly to match the experimental data, or that the resolution is not sufficient to resolve all stable period dynamics. This heavily contributes to the large underestimation of the stability at night, as depicted by the Obukhov length. The data from Hicks [46] indicates that the stability at night is strongly stable which is not captured by the LES. The LES predicted stability is still very stable. Fig. 4.4e and f shows that the wind direction follows qualitative behaviors compared to the Wangara data [28]. During the convective period, the wind points to the north west and rotates toward the east as the night evolves. A more detailed comparison for the time series data is given for the convective and stable regimes in sections 4.3 and 4.4, respectively.

As mentioned prior, moisture statistics were calculated. However, the velocity and temperature results were only weakly dependent on moisture effects due to the dry conditions. A test simulation neglecting moisture was performed to validate that moisture had only a slight impact on the system. Furthermore, due to neglecting advection, evaporation, and condensation to the ground in the case setup, the computational results for moisture are not expected to match experimental data. Discrepancies between the experimental data and this LES results were observed. Therefore, following to the approach of Yamada and Mellor [106] these results are not included in the body of this text.

4.2 AMR behavior

Before discussing the results of the AMR simulation versus static LES, an understanding of the vertical grid spacings resultant from the AMR procedure is required. Fig. 4.5 depicts time height plots of the vertical grid spacing saved every 5 minutes of simulated time. This figure and the results in sections 4.3 and 4.4 were generated with Eq. (3.18) with $\lambda_1 = 1$, $\lambda_2 = 6$, and $\lambda_3 = 1$. λ_2 was chosen to place emphasis on temperature gradients, specifically those associated with the entrainment zone. Overlaid on Fig. 4.5 is the estimated boundary layer height. During the convective period, the criteria provides increased resolution near the land surface. This is an important trait of an LES grid, as recently shown by Degrazia et al. [34]. They determined that because of the reduction in characteristic turbulent vertical length scales near the ground, the grid spacing is this region should be reduced to decrease the LES filter width and lessen the dependence on SGS parameterizations. Away from the ground, the criteria causes equally spaced vertical points throughout the well-mixed

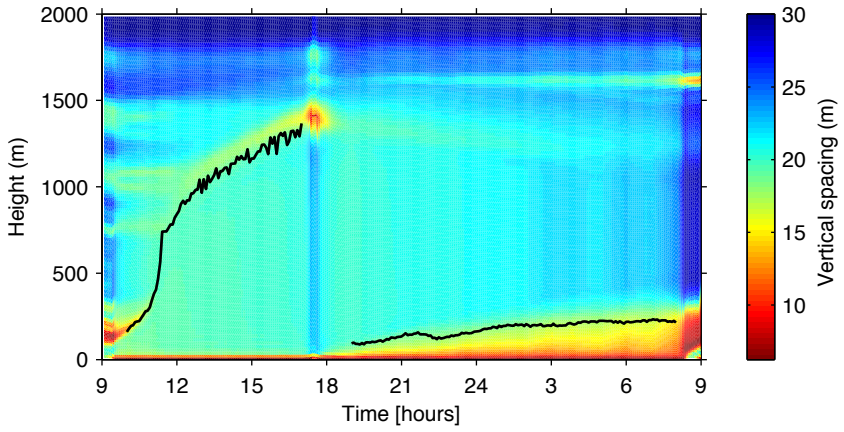

Figure 4.5. Behavior of the AMR criteria of Eq. (3.18). The contour plot shows vertical resolution (m) profiles every 5 minutes. The LES computed boundary layer height (——) is overlaid for reference excluding the transitions.

CBL where the vertical length scales are bigger and large, coherent structures dominate the physics. Points are also clustered in the entrainment zone and decreased above the CBL. Vertical resolution in the entrainment zone is important to control overentrainment [97, 92, 24]. Furthermore, LES has been found to be less sensitive to horizontal resolution in the entrainment zone [62, 92]. During the stable period, grid points are clustered in the SBL and expanded through the residual layer into very coarse spacing in the sponge layer. Increased resolution in the SBL has been found to be critical in sustaining resolved turbulence and to accurately represent stratified motions [15, 12].

4.3 Convective regime

To begin the examination of the convective time period, time series data of the CBL height, surface sensible heat flux, surface friction velocity and near surface wind direction are presented in Fig. 4.6. For the CBL height and surface sensible heat flux series, the AMR simulation exhibits magnitudes and behaviors closer to the 192^3 simulation than the 96^3 static simulation. The CBL height predicted by the AMR simulation matches well with the 192^3 simulation results while the 96^3 static simulation consistently underestimates the CBL height. The 96^3 static simulation also underestimates the surface sensible heat flux compared to the 192^3 simulation results (over 20 percent in the early afternoon). The 192^3 simulation has a near constant trend throughout the afternoon and the AMR simulation has a decreasing trend beginning around 1200 LST. In contrast, the 96^3 static simulation shows a period of increasing flux between 1350-1600 LST. Around 1500 LST the 96^3 simulation's heat flux crosses the others followed by a drop off of all three at the onset of transition. The opposing trends of the simulations suggests that the 96^3 static simulation does not begin to perform better as the CBL grows, but rather that the heat flux profiles are simply crossing.

The surface sensible heat flux and CBL height are heavily influenced by the surface layer resolution and nature of the boundary condition, which is directly dependent on the height of z_1, and therefore the prescribed surface temperature. The simulations with nodes closer to the ground respond quicker to surface changes and have a larger positive heat flux throughout the convective regime. These stronger heat fluxes act to add more energy to the system, fueling warmer air and convective plumes to push the height of the CBL higher. The convective velocity scales, w_* were calculated (not shown) and found to be on the order of 1-2 m s^{-1} signifying the vigorous heating and strong convective conditions [96]. The 192^3 and AMR simulations exhibited larger magnitudes of w_* for most of the day, indicative of the large scale structures resulting in increased CBL height compared to the

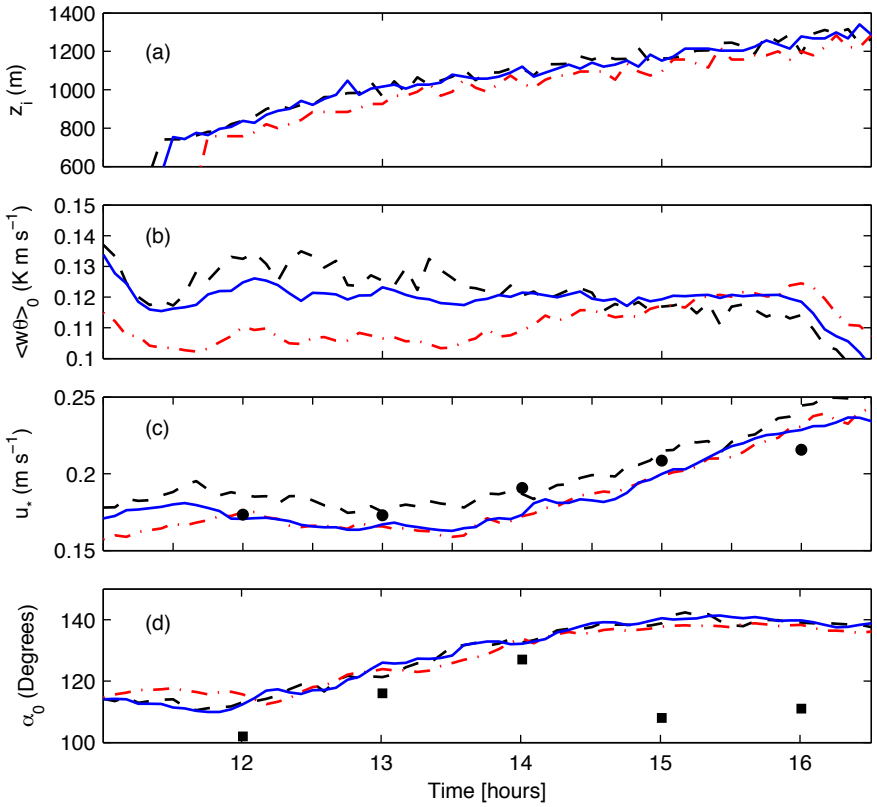

Figure 4.6. Comparisons of the LES time series of boundary layer height, z_i (a), surface sensible heat flux, $\langle w\theta \rangle_0$ (b), surface friction velocity, u_* (c), and wind direction, α_0 (d) with corresponding Clarke data ($C71_0$). Line types are as follows: AMR (– –), 96^3 (–·–), 192^3 (——), H81(▪), and $C71_0$(•).

static 96^3 simulation.

The surface friction velocity, depicted in Fig. 4.6c, is larger in magnitude for the AMR simulation than the 96^3 and 192^3 simulations. This behavior is strongly linked to SGS model behavior and grid anisotropy. This will be explored further below when discussing variances. In Fig. 4.6c, all simulations exhibit the same temporal trends for u_*, generally increasing throughout the period. In Fig. 4.6d the ground level wind direction is provided, which is representative all heights. This is not heavily influenced by resolution during the convective regime as all simulations have good collapse.

Figs. 4.7 and 4.8 show the mean velocity and potential temperature vertical profiles from the convective regime for the vertical AMR and static grid simulations. The profiles are averaged over horizontal planes and in time for three representative one hour periods. In Fig. 4.7, u profiles indicate that the AMR simulation underestimates the u velocity but still matches the 192^3 simulation better than the 96^3 static simulation. This is especially true in the surface layer and entrainment zone of the simulations. The static 96^3 simulation consistently overestimates the u velocity magnitude throughout the convective regime, with the percentage of difference decreasing as the CBL develops. This is an indication of a faster acceleration in the AMR and 192^3 simulations resultant from the geostrophic forcings. Other impacting factors could be the improved coupling from the finer grid spacings in the AMR simulation, and the increased mixing that would result from the increased surface sensible heat flux depicted in Fig. 4.6b. This should not be interpreted as the static 96^3 resolution simulation performing more like the 192^3 simulation as the CBL develops. In the v profiles similar observations are evident, however the differences are not as dramatic. The entrainment region does not demonstrate the same degree of similarity between the AMR and 192^3 simulations as was observed in the u velocity. Just below the entrainment zone the AMR simulation does do a better job reproducing the 192^3 simulation profile compared to the static 96^3 simulation.

The potential temperature vertical profiles shown in Fig. 4.8 clearly display a strength of the AMR simulation. The AMR simulation more closely matches the warmer temperature profile of the 192^3 simulation than does the static 96^3 simulation. The sensible heat fluxes depicted in Fig. 4.8 indicate that the close match in potential temperature between the AMR and the 192^3 simulation can be attributed to the much closer match in sensible heat flux. Specifically, at z_1, the larger heat fluxes of the AMR and 192^3 simulations result in raised air temperatures near the surface and subsequently the entire boundary layer, as supported by Fig. 4.6b. In general, by examining the mixed layer in all three simulations,

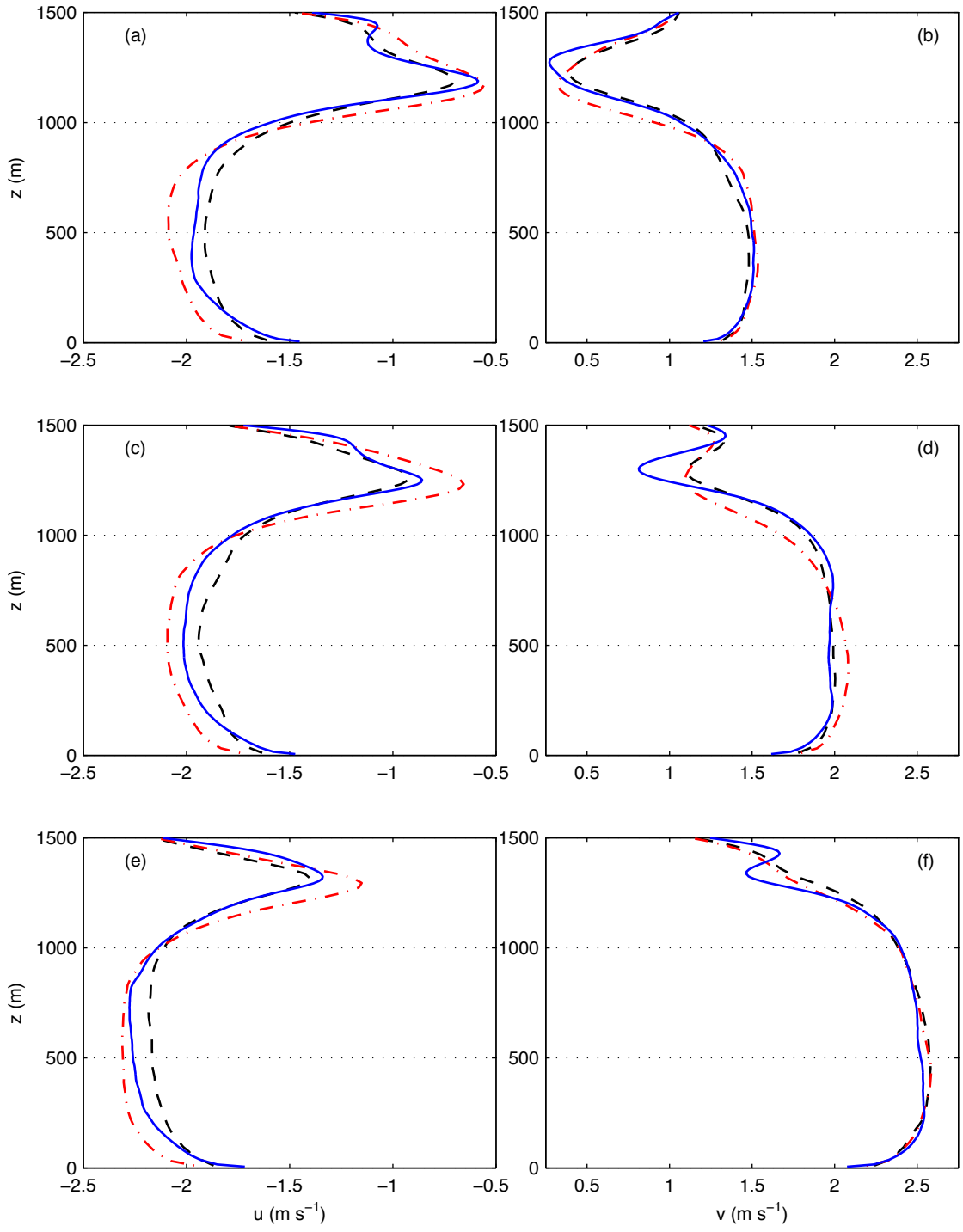

Figure 4.7. Comparison of LES u, (a,c,e) and v (b,d,f), velocity components during the convective regime. Hourly averages are from top to bottom: 1300-1400 LST (a,b), 1400-1500 LST (c,d), and 1500-1600 LST (e,f). Line types are as follows: AMR (— —), 96^3 (– · –), 192^3 (——).

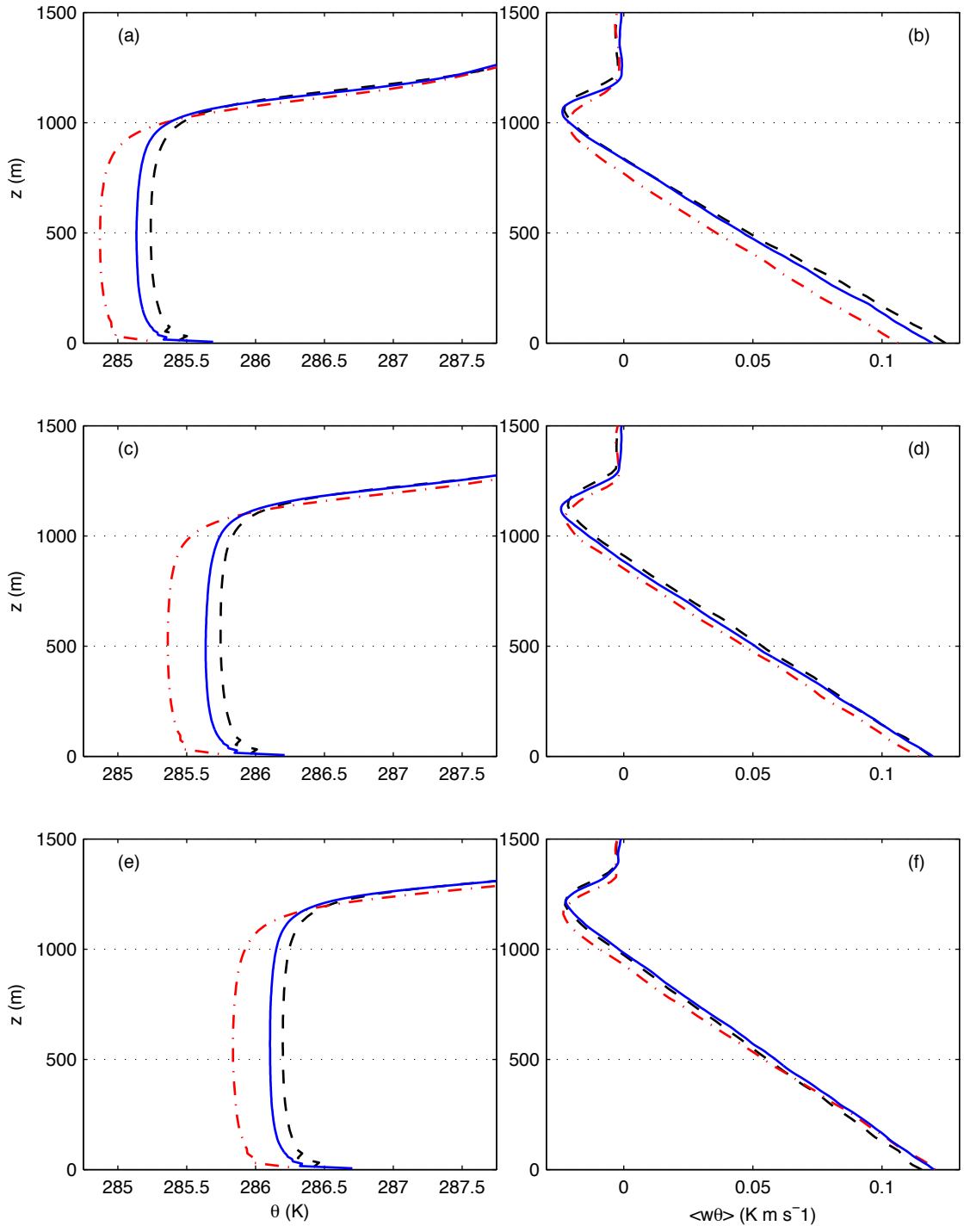

Figure 4.8. Comparison of LES θ (a,c,e) and total sensible heat flux $\langle w\theta \rangle$ (b,d,f) during the convective regime. Hourly averages are from top to bottom: 1300-1400 LST (a,b), 1400-1500 LST (c,d), and 1500-1600 LST (e,f). Line types are as follows: AMR (– –), 96^3 (–·–), 192^3 (——).

there does not appear to be a strong dependance of the mean potential temperature and flux profiles on either vertical or horizontal resolution. For the simulations tested here, the shapes and slopes of the potential temperature and flux profiles in the mixed layer all have the same general trends, albeit different magnitudes. This is a positive result considering that while the AMR does have a finer vertical spacing throughout the mixed layer compared to the static 96^3 simulation, it is still coarser than the 192^3 simulation. The AMR simulation vertical spacings range between 19.5-20.5 m in the mixed layer, as dictated by the AMR criteria. Overall, AMR is able to efficiently allocate resources in the mixed layer and focus resolution in other areas providing improved results.

In the entrainment zone, the AMR matches the 192^3 resolution results for the entrainment zone size, shape, and sensible heat flux magnitude better than the 96^3 static resolution. The non-dimensional sensible heat flux profile in Fig. 4.9 confirms that increased vertical resolution in the entrainment zone leads to a sharper flux profile over a more compact vertical region with more distinct boundaries. Sullivan and Patton [98] found similar results in their CBL study. The AMR simulation achieves these characteristics due to the propagating effects from the larger surface flux and the resolution increase in the entrainment region. The large temperature gradients present in the entrainment zone, coupled with the third term in the AMR criteria of Eq. (3.18) causes a reduction in the vertical grid spacings, with Δz reduced to a range between 16.5-19 m. This results in better resolution of the gradients and hence an approximation closer to the 192^3 simulation. Cloud resolving studies often use increased resolution determined *a priori* in the entrainment zone to provide better simulations [97, 92, 24]. Since the boundary layer height is constantly changing in the unsteady CBL, the AMR is advantageous in avoiding an *a priori* estimate of the location of the entrainment zone, as proven here.

Typical values for the ratio between surface and maximum entrainment heat flux ranges between 0.1-0.3 [96] for a case of free convection. All simulations tested here have a value very close to the median of 0.2. The AMR simulation has the lowest of the simulations and does does not match the 192^3 as well as the 96^3 simulations. This is attributed to the effect of increased vertical resolution near the surface, compared to the effect of increased vertical resolution in the entrainment zone. Increased resolution near the surface has a strong impact on the value of the surface sensible heat flux as seen in Fig. 4.8. Increased vertical resolution in the entrainment zone also impacts the heat flux, however the impact on the magnitude does not seem to be as dramatic as in the surface layer. Therefore, the ratio of the two fluxes for the AMR simulation seem to reveal the varying degree of influence

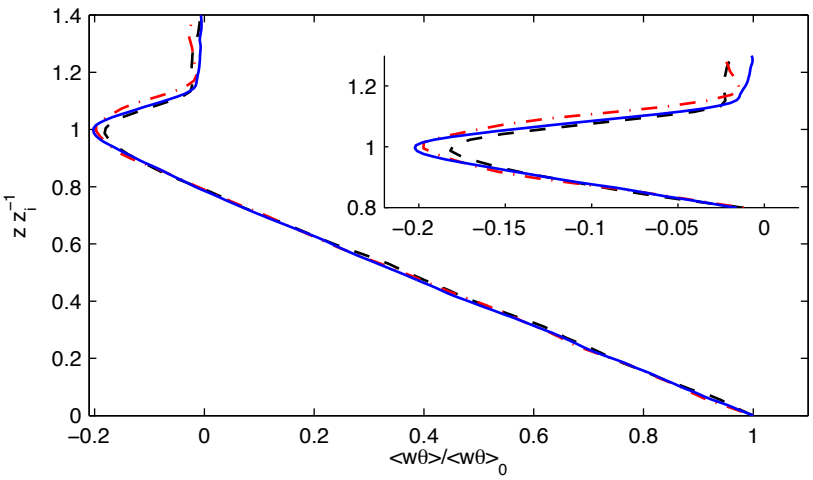

Figure 4.9. Comparison of LES nondimensional total sensible heat flux $\langle w\theta \rangle \, \langle w\theta \rangle_0^{-1}$ during the convective regime. An insert is provided to enlarge the entrainment zone. Hourly average is for 1400-1500 LST. Line types are as follows: AMR (– –), 96^3 (– · –), 192^3 (——).

the AMR has at different locations in the simulation domain.

Second- and third-order statistics are given in Figs. 4.10 and 4.11. In addition to the 192^3, 96^3 static, and AMR cases, Figs. 4.10 and 4.11 also include results from the static simulation that has been refined by a factor of two in the z direction, i.e., the $96 \times 96 \times 192$ grid point simulation. Fig. 4.10 shows the total variances of the horizontal and vertical velocities and the potential temperature. Note that the streamwise and spanwise variances are nearly identical and have therefore, been combined. Following Sullivan and Patton [98], the total horizontal variance is defined as $\sigma_h = \sigma_{\tilde{u}} + \sigma_{\tilde{v}} + 4e/3$, the total vertical variance as $\sigma_w = \sigma_{\tilde{w}} + 2e/3$, and the total potential temperature variance as $\sigma_\theta = \sigma_{\tilde{\theta}} + e_\theta$, where e is the SGS turbulent kinetic energy (TKE) and e_θ is SGS scalar variance [65].

The velocity and potential temperature total variances for all simulations exhibit the expected trends for a convective regime according to mixed scaling hypotheses as discussed in Schmidt and Schumann [84]. In Fig. 4.10 the horizontal velocity variances have a nearly constant value through the mixed layer with good collapse across all simulations. In the entrainment zone, a maxima is observed with a magnitude of approximately 0.5. The AMR simulation has a maxima closer to the 192^3 simulation. Although the AMR simulation maxima matches the 192^3 case, the peaks in the variance are not as sharp. This is true for all the low resolution simulations. The shape of the variance indicates a broader, less distinctly defined entrainment zone for the 96^3 static, AMR and $96 \times 96 \times 192$ simulations. This agrees with the heat flux profiles in Fig. 4.9 where the 96^3 static and $96 \times 96 \times 192$ static simulations have broader entrainment regions. Sharper variance peaks were also observed by Sullivan and Patton [98] with increased resolution, suggesting that the vertical AMR used here, although providing some improvement, is not enough to match higher resolution simulations in the entrainment zone. This indicates that either more refinement would be required in the vertical direction, or that horizontal refinement is also necessary to improve second-order statistics.

In Figs. 4.10a and c, the 192^3 resolution simulation has the largest magnitude of the total horizontal variance peak in the entrainment zone. At the end of the convective period, the 192^3 simulation has the smallest total horizontal variance peak in the entrainment zone. The 96^3 static simulation has an opposite trend. It has the lowest total horizontal variance peak in Figs. 4.10a and c. In Figs. 4.10e, the variance has increased from previous hours and is larger than the 192^3 simulation results. The AMR simulation has a trend similar to the 192^3 simulation. This further indicates that the AMR results improves the representation in the entrainment zone. It is also interesting to note the $96 \times 96 \times 192$ simulation produces

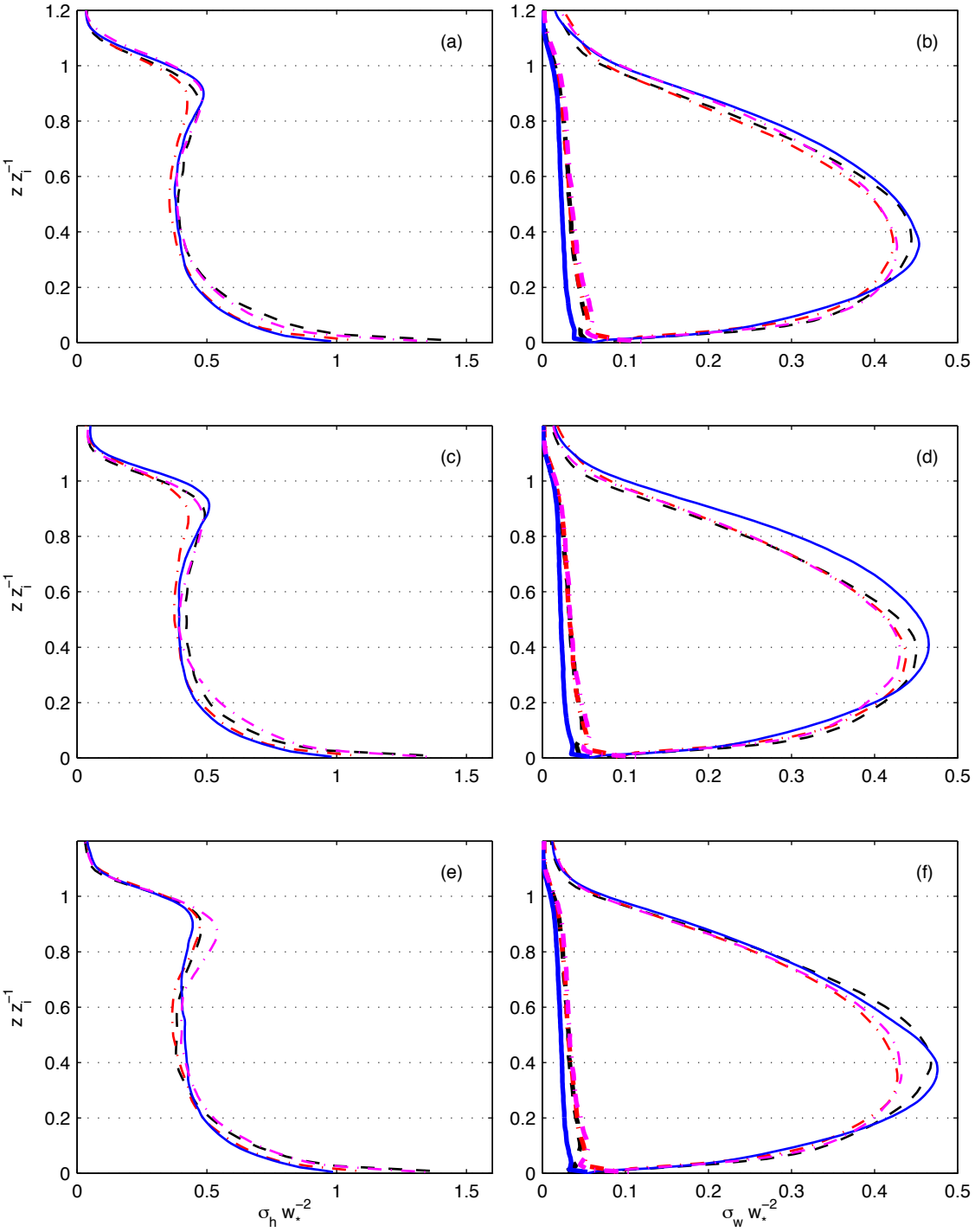

Figure 4.10. Comparison of LES total horizontal variances $\sigma_h w_*^{-2}$ (a,c,e) and vertical variance $\sigma_w w_*^{-2}$ (b,d,e) during the convective regime. Hourly averages are from top to bottom: 1300-1400 LST (a,b), 1400-1500 LST (c,d), and 1500-1600 LST (e,f). Line types are as follows: AMR (– –), 96^3 (–·–), 192^3 (——), $96 \times 96 \times 192$ (–··–). Thick lines are SGS vertical variance contribution.

in increase an the total horizontal velocity variance in the entrainment zone between Fig. 4.10c and e. This behavior is more like the low resolution simulation.

A more striking difference is observed near the ground between the AMR simulation and the other 96^3 and 192^3 simulations. The AMR simulation has a much larger resolved variance. This is an artifact of surface layer grid resolution and grid aspect ratio. This conclusion is supported by the similar behavior of the $96 \times 96 \times 192$ static simulation, which also has a higher grid aspect ratio. This suggests that there is a limit on the acceptable aspect ratio for proper performance of the SGS model used in this study. Similar increased total horizontal variances were observed by Degrazia et al. [34] who used a stretched vertical grid to simulate the CBL. This behavior is linked to the nature of the boundary condition. Stoll and Porté-Agel [94] examined the influence of changing surface roughness in the boundary layer parameterization in a neutral flow. They found that increased surface roughness resulted in lower total streamwise velocity variance at z_1 due to increased fluctuations in the surface shear stress which damps fluctuations in the resolved velocity. Since the denominator of the momentum boundary condition contains the term

$$\ln\left(\frac{z_1}{z_0}\right), \tag{4.1}$$

it can be anticipated that a decrease in z_1 would have a similar impact on the boundary condition as increasing z_0. This is a reasonable assumption even with the presence of the other terms that affect the boundary condition (Eq. (3.21). By examining the total horizontal velocity variance at z_1, similar behavior to that of Stoll and Porté-Agel [94] is observed for the 96^3 and 192^3 static simulations. The 192^3 simulation has a lower total horizontal variance at z_1. The AMR and $96 \times 96 \times 192$ simulations do follow this behavior and have large total horizontal velocity variance at z_1. This indicates that the aspect ratio is also contributing to the behavior of the boundary conditions and indicates the sensitivity of the boundary conditions to both z_1 and the grid resolution in the surface layer. This behavior agrees with the friction velocity series observed in Fig. 4.6. The $96 \times 96 \times 192$ simulation is not shown but had magnitudes similar to that of the AMR simulation.

The total potential temperature variance in Fig. 4.11 has similar characteristics and behaviors to the total horizontal variances. There is an increase in total variance in the surface layer for the AMR and $96 \times 96 \times 192$ static simulations, and good collapse of all simulations in the mixed layer. The AMR results match the peak magnitude and shape of the total potential temperature variance of the 192^3 simulation in the entrainment zone better than the 96^3 static case.

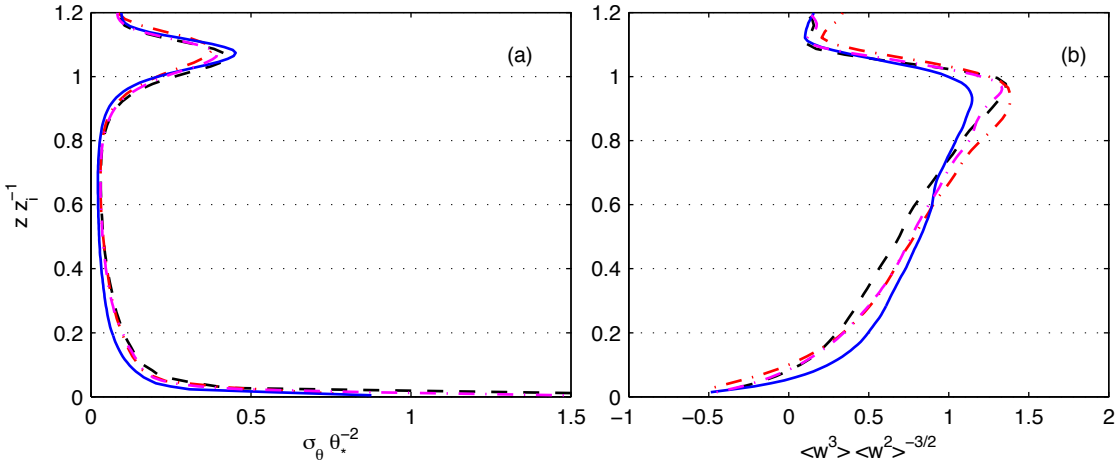

Figure 4.11. Comparison of LES total potential temperature variance $\sigma_\theta \theta_*^{-2}$ (a) and LES resolved vertical velocity skewness $\langle w^3 \rangle \langle w^2 \rangle^{-3/2}$ (b) during the convective regime. An insert is provided to enlarge the entrainment regions of the potential temperature variance. The hourly average of both plots is between 1400-1500 LST. Line types are as follows: AMR (— —), 96^3 (– · –), 192^3 (——), $96 \times 96 \times 192$ (– · –)

The total vertical velocity variance in Fig. 4.10 behaves as expected [84]. It has a horizontally rounded profile with peaks at approximately $z = H/3$. The 192^3 simulation has greater total vertical velocity variance than the lower resolution simulations. This trend has been previously observed from other LES studies [68, 98]. The SGS contributions to vertical velocity variance are also included in Fig. 4.10. As expected, the SGS contribution is increased with lower resolution. Similar to what Moeng et al. [68] found, this difference is not enough to compensate in the 96^3 and $96 \times 96 \times 192$ simulations to equal the total vertical velocity variance of the 192^3 simulation. The AMR simulation consistently matches the 192^3 simulation better, indicating that the AMR simulation has an increased resolution of turbulence in the vertical direction. Interestingly, the AMR simulation matches the high resolution total variance better than the 96^3 static and $96 \times 96 \times 192$ cases despite the latter having a finer vertical resolution in the mixed layer.

The resolved vertical velocity skewness, defined as $\langle w^3 \rangle \langle w^2 \rangle^{-3/2}$, is depicted in Fig. 4.11. This provides understanding about the influence of AMR on third-order statistics. The results indicate that all of the simulations with horizontal resolutions of 96^2 points perform very similar to each other and that all deviate from the 192^3 simulation skewness profile. Near the ground, the skewness is unrealistically negative in all simulations. The 192^3 simulation becomes positive at a lower height than the other simulations, a behavior also observed by Sullivan and Patton [98]. Schmidt and Schumann [84] concluded in their study of LES of the CBL that negative third-order moments resulted from an imbalance between the SGS model dissipation (both within the mixed layer and lowest grid cell) and the surface boundary condition (with the surface roughness exhibiting direct impact on the skewness). Hence, this sensitive balance is not achieved in this LES study, as seen in most LES studies. However, Schmidt and Schumann [84] also state that this issue does not appear to cause deficiencies in the bulk results of the CBL.

Through the mixed layer the skewness increases in magnitude with a constant slope up to a maximum between 80-100 percent of the CLB height. The 192^3 simulation has a steeper slope and a maximum skewness magnitude of approximately 1.0, while the other simulations have more mild slopes and greater maximums. Sullivan and Patton [98] also found that with increased resolution the profiles had an earlier transition to positive values and steeper slopes up to the entrainment zone. Considering their findings and those seen in this study, the vertical velocity skewness does not appear to be very sensitive to the increase in vertical grid spacing as evidenced by the $96 \times 96 \times 192$ and AMR simulations. Rather, the horizontal spacing controls the behavior of the profile. This is somewhat intuitive since

the vertical velocity skewness describes the ratio of upward to downward motions, which are primarily detectable in horizontal spacings. These behaviors suggest that the vertical AMR is not sufficient to cause significant improvements in third-order statistics.

4.4 Stable regime

In section 4.3 it was found that during the daytime convective period, first- and second-order statistics are the most sensitive to vertical resolution in the near surface and entrainment regions. In these regions, the use of vertical AMR improved the agreement between high resolution and low resolution with AMR simulations. In this section, simulation statistics from the nighttime stable period of the diurnal cycle are examined and the performance of the vertical AMR simulation is evaluated. In addition to the static grid simulations of 96^3 and 192^3 grid points, results from the simulation that used $96 \times 96 \times 192$ grid points are included in all stable regime figures. To begin, in Fig. 4.12 the horizontally averaged SBL height, surface sensible heat flux, surface friction velocity, and surface wind direction time series for the nighttime hours between 2000 LST and 0600 LST. In contrast to Fig. 4.6 where the CBL height predicted from the 96^3 vertical AMR simulation matched the 192^3 simulation better than 96^3 static grid simulation, in Fig. 4.12a there is little difference in SBL heights between the 96^3 static and 96^3 AMR simulations. Both 96^3 simulations substantially overestimate the height throughout the stable regime compared to the 192^3 simulation results. The AMR simulation has the highest SBL height after the transition, but improves to follow the $96 \times 96 \times 192$ and more closely match the 192^3 simulation throughout the night compared to the 96^3 static simulation. The surface friction velocity and surface sensible heat flux are also improved by vertical AMR with respect to agreement with the 192^3 case compared to the 96^3 and $96 \times 96 \times 192$ static simulations throughout most of the stable regime. Near the ground the wind direction has more resolution dependence during the stable regime than was observed during the convective regime. The use of the dynamic grid improves the agreement between the 96^3 AMR and 192^3 simulations compared to the 96^3 and $96 \times 96 \times 192$ static simulations. The 192^3 simulation rotates the least towards the east. Above the ground (not shown) the wind direction has less dependence on resolution and all simulations produce nearly identical wind directions.

Fig. 4.13 shows the horizontally and time averaged vertical profiles of the mean wind speed alongside the total momentum flux, u_{*L}^2. Three hourly averages are plotted including hours 2000-2100 LST (a,b), 2300-2400 LST (c,d) and 0200-0300 LST (e,f) that represent the typical behavior of the early, middle and late stable periods, respectively.

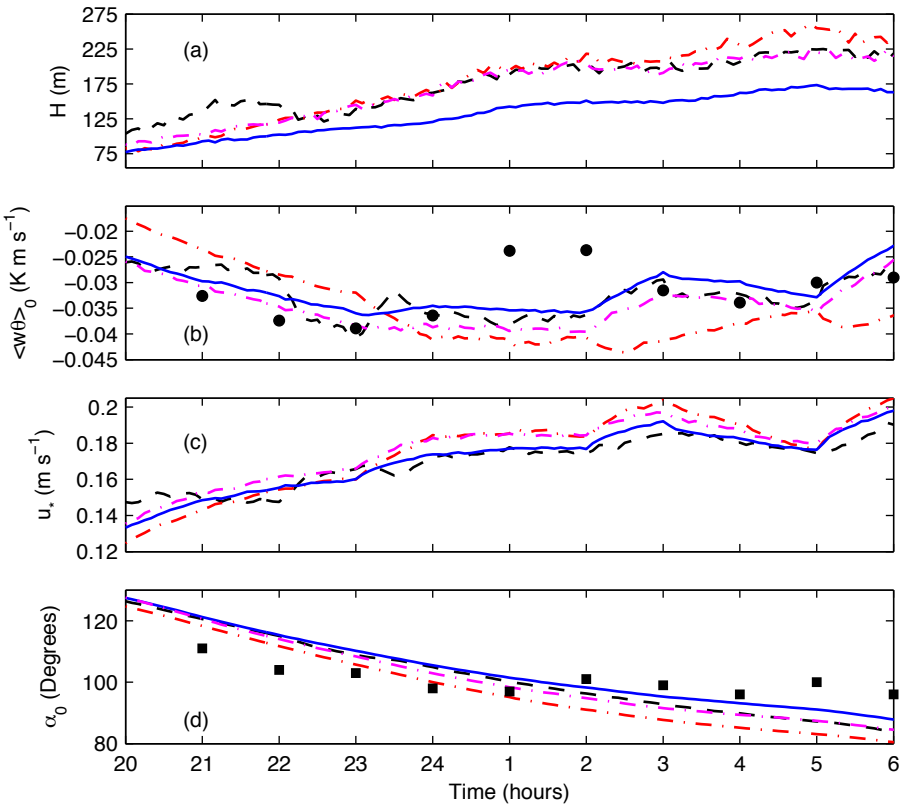

Figure 4.12. Comparisons of the LES time series for the stable regime of boundary layer height, H (a), surface sensible heat flux, $\langle w\theta \rangle_0$ (b), surface friction velocity, u_* (c), Obukhov length, and near surface wind direction, α with corresponding Clarke data $C71_0$. Line types are as follows: AMR (— —), 96^3 (– · –), 192^3 (——), $96 \times 96 \times 192$ (– · –), H81(▪), and $C71_0$(•).

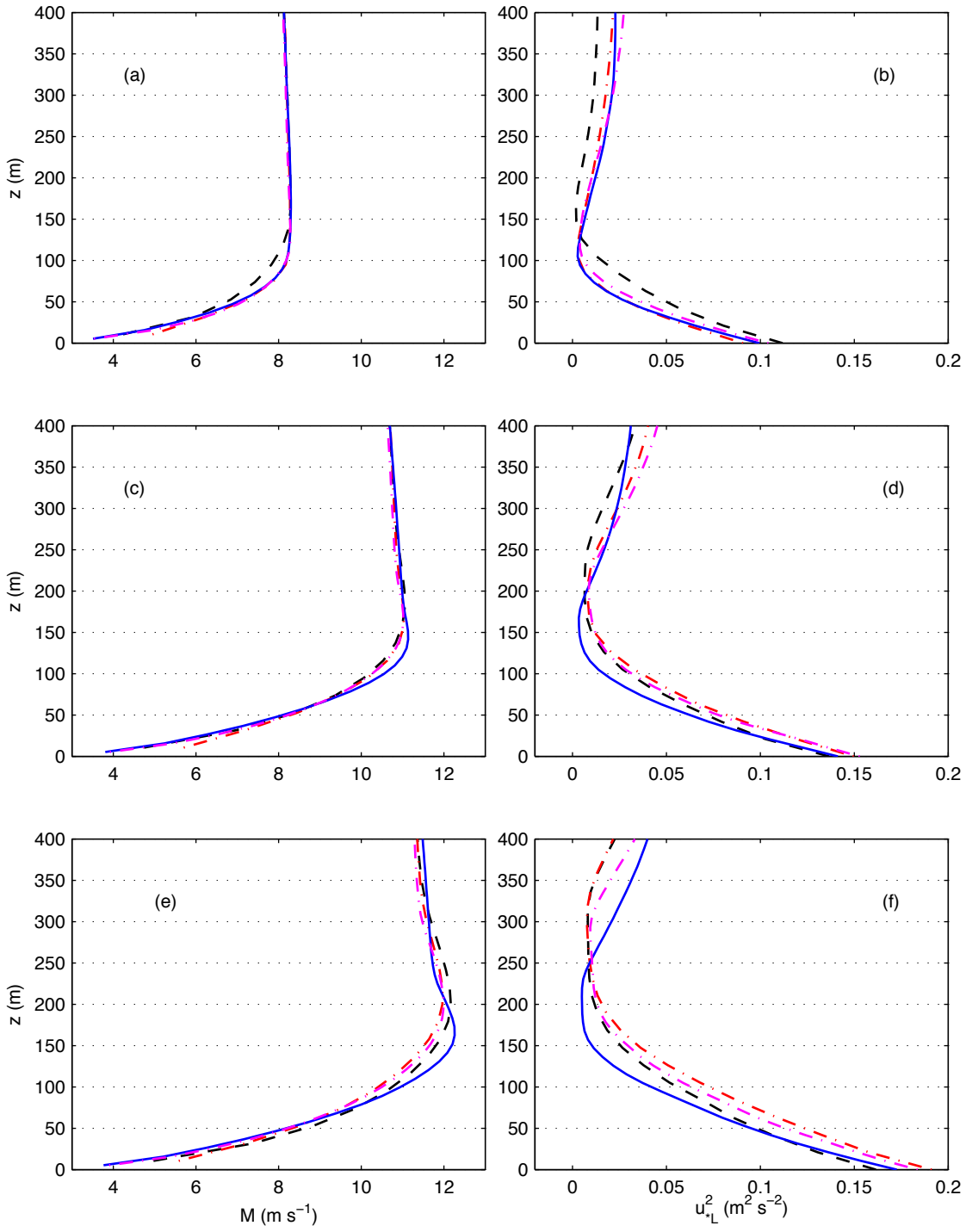

Figure 4.13. Comparison of LES mean wind speed and total momentum flux during the stable regime. Hourly averages are between 2000-2100 LST (a,b), 2300-2400 LST (c,d), and 0200-0300 LST (e,f). Line types are as follows: AMR (– –), 96^3 (–·–), 192^3 (——), $96 \times 96 \times 192$ (–·–)

In the early and middle periods of the stable regime, the AMR simulated mean wind speed matches the 192^3 case well near the surface. In Fig. 4.13a and Fig. 4.13c the 96^3 static simulation overestimates the wind speed near the surface. However, during the early hours of the stable period the AMR simulation exhibits the slowest wind speed of the simulations further away from the ground. Fig. 4.13b shows that the momentum flux in the AMR simulation results is larger than the other simulations, indicating that there is stronger mixing and turbulence. The excessive mixing leads to reduced gradients potentially causing the discrepancy in mean wind profiles. Between 2300-2400 LST, away from the ground the AMR simulation has accelerated and has a wind speed profile closer to the 96^3 and $96 \times 96 \times 192$ simulations. At this time the LLJ has begun to form and it is noteworthy that the early LLJ peak from the AMR simulation has a nearly equal, yet higher height of the peak than the 96^3 and $96 \times 96 \times 192$ simulations. The momentum flux has adapted in the AMR simulation to more closely resemble the 192^3 simulation. During the late stable period, as the AMR simulation momentum flux continues to more closely match the higher resolution simulation, the LLJ peak magnitude of the AMR simulation is increasingly more like the 192^3 simulation and the peak height has lowered to be equal to that of the 96^3 and $96 \times 96 \times 192$ simulations. The 192^3 simulation has a lower and sharper LLJ peak than the 96^3 static, AMR, and $96 \times 96 \times 192$ simulations during both the middle and late stable periods.

In Fig. 4.14 the mean potential temperature and sensible heat flux profiles are presented. The AMR simulation results are a closer match than the 96^3 static simulation to the 192^3 simulated potential temperature profile in the lower half of the SBL throughout the stable regime. At approximately 50 percent of the SBL height, the AMR profile begins to converge more to the warmer 96^3 static simulation results in all of the stable periods. The $96 \times 96 \times 192$ simulation performed similarly, except its potential temperature does not deviate as much as the AMR simulation from the 192^3 simulation in the top half of the SBL. Throughout the SBL, the 96^3 static, AMR, and $96 \times 96 \times 192$ simulations all have reduced potential temperatures gradient up to the residual layer compared to the 192^3 simulation. This suggests excessive mixing in the SBL for the 96^3 static, AMR, and $96 \times 96 \times 192$ simulations. The average sensible heat flux presented in Fig. 4.14 supports this. In the middle and late stable periods, the 192^3 simulation has a lower magnitude of vertical sensible heat flux than the other simulations resulting in a cooler, less mixed SBL. The greater mixing in the lower resolution simulations brings warmer air from the residual layer above into the SBL which also serves to partly explain the discrepancies between the SBL heights shown in

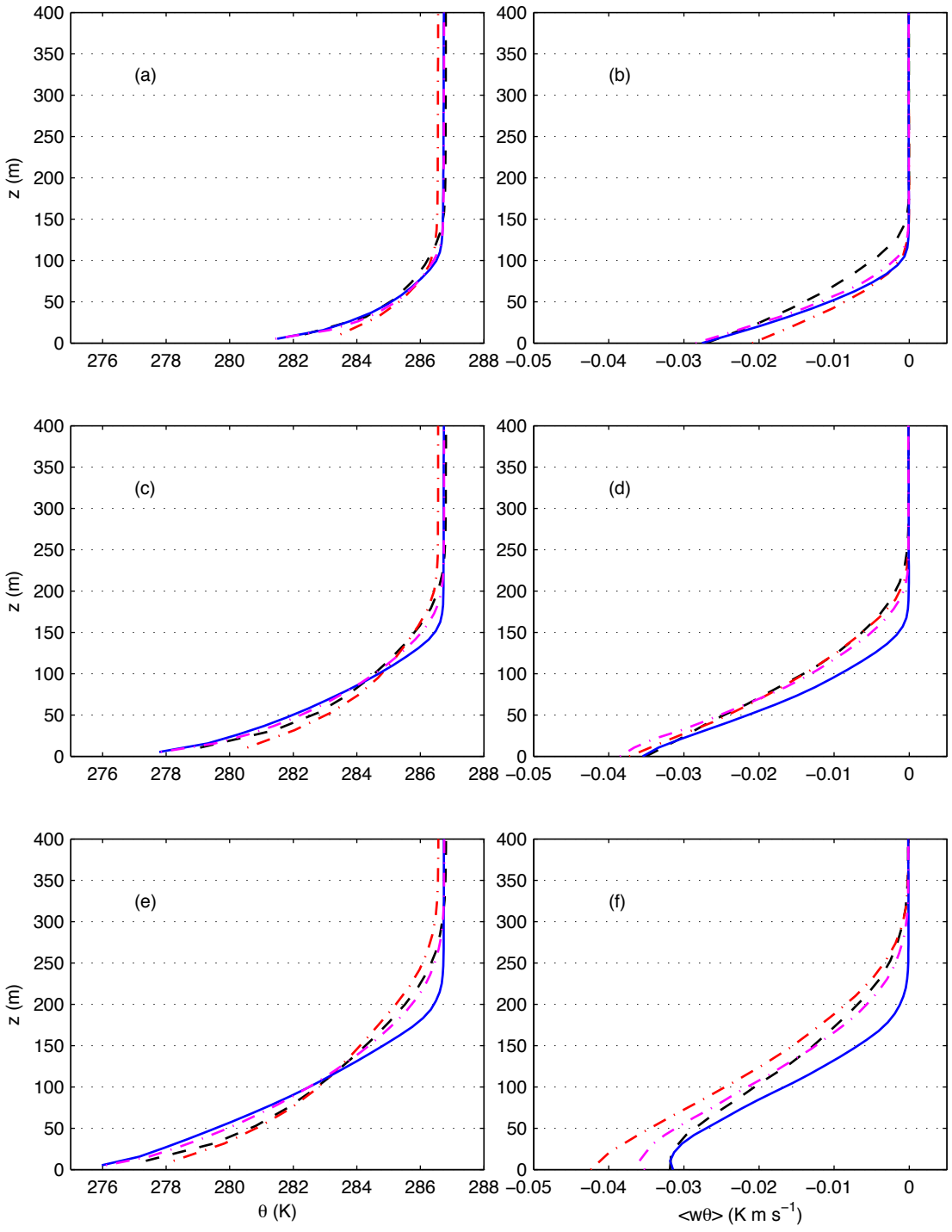

Figure 4.14. Comparison of LES potential temperature, θ (a,c,e) and sensible heat flux, $\langle w\theta \rangle$ (b,d,f). Hourly averages are between 2000-2100 LST (a,b), 2300-2400 LST (c,d), and 0200-0300 LST (e,f). Line types are as follows: AMR (– –), 96^3 (–·–), 192^3 (——), $96 \times 96 \times 192$ (–·–)

Fig. 4.12a. Near the surface, as discussed previously from Fig. 4.12, the AMR simulation does a better job of matching the 192^3 simulation sensible heat flux compared to the static 96^3 simulation. The sensitivity of the vertical flux profile to the surface condition and near surface resolution is further evident in Fig. 4.14f. At 0200 LST there is a slight increase in the prescribed surface temperature which results in an increase in surface sensible heat flux. The $96 \times 96 \times 192$, AMR, and 192^3 simulations reflect this change immediately. In contrast, the 96^3 simulation lags the increase in surface sensible heat flux by 30 minutes causing a difference in the profile shape between 0200-0300 LST in the lowest 40 m.

These first-order averages and corresponding fluxes establish that vertical resolution plays an important role in the SBL. They also indicate that sufficient horizontal resolution is significant. The AMR and $96 \times 96 \times 192$ simulation results are evidence of the impact that increased vertical resolution can have, specifically as provided through AMR. Comparing the two directly suggests that a more robust AMR criteria would be able to improve results towards the top of the SBL. However, the $96 \times 96 \times 192$ simulation reveals that the improvements would be marginal and that it would be more influencial to provide AMR in the horizontal directions as well.

Fig. 4.15 shows the normalized momentum and sensible heat flux profiles. In a continuously turbulent SBL, Nieuwstadt's local scaling hypothesis [73] predicts that the momentum flux should scale as z/H to the 3/2 power and that the sensible heat flux should scale linearly with z/H. The normalized momentum scaling, depicted in Fig. 4.15a for the early, middle and late stable periods, indicates that the momentum scaling holds well for the evolving SBL simulated here. The sensible heat flux in Fig. 4.15b, portrays the early and middle periods of the stable regime. The sensible heat flux scaling generally holds, however the vertical profiles from the simulations do show more curvature than expected for linear scaling. Fig 4.15c shows the normalized sensible heat flux profile between 0200-0300 LST. During this time period, the surface heat flux changes becoming less negative as the prescribed surface temperature briefly increases. This was also observed in Fig. 4.12b. Because of this temporal evolution, during this period the SBL does not scale as observed in Nieuwstadt [73], which was a continuously cooling SBL case. Still, it is evident that in this study Neiuwstadt's local scaling does hold at other periods (Fig. 4.15b). Therefore, caution should be taken in the averaging and reviewing of SBL evolution and scaling statistics to ensure correct trends are captured. In fact, the 96^3 static simulation could be considered to agree with local scaling better than the AMR and higher resolution simulations based on Fig. 4.15c. In actuality, it is a lag in the evolution of the surface sensible heat flux for

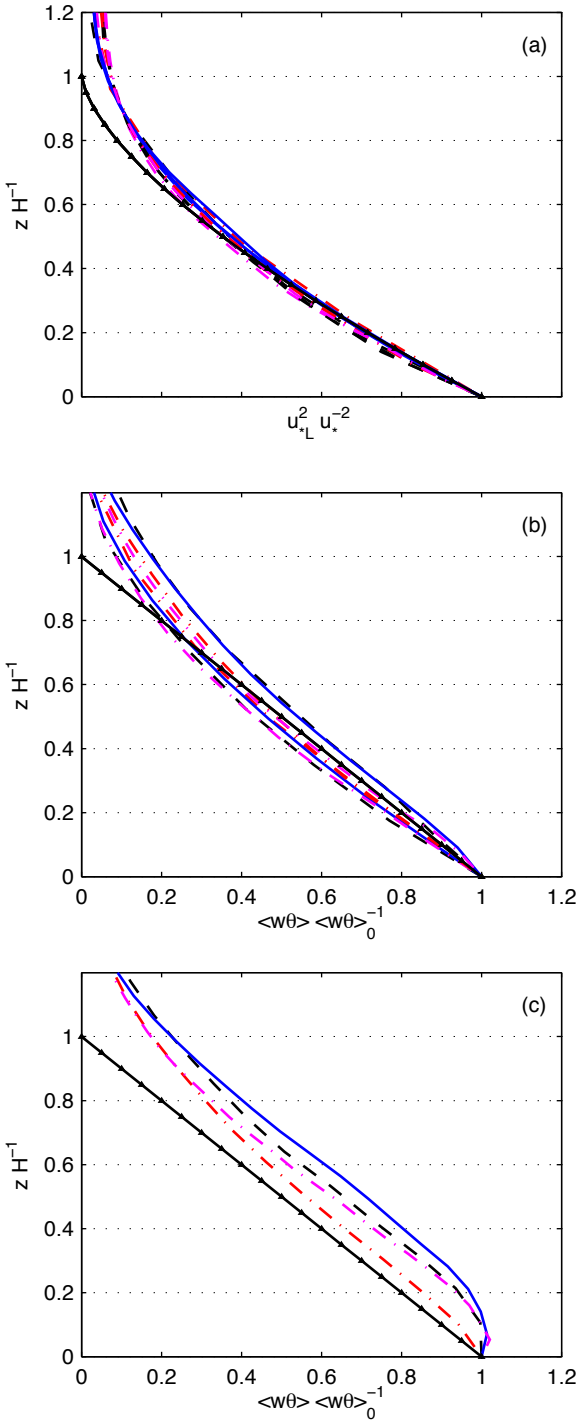

Figure 4.15. Comparison of LES normalized momentum flux $u_{*L}^2 u_*^{-2}$ (a) and normalized sensible heat flux, $\langle w\theta \rangle \langle w\theta \rangle_0^{-1}$ (b,c) during the stable regime. Plot (a) contains profiles averaged between 2000-2100 LST, 2300-2400 LST, and 0200-0300 LST. Plot (b) contains profiles averaged between 2000-2100 LST and 2300-2400 LST. Plot (c) contains profiles averaged between 0200-0300 LST. Line types are as follows: AMR (— —), 96^3 (– · –), 192^3 (——), $96 \times 96 \times 192$ (– · –), and Nieuwstadt [73] (●——●)

the 96^3 static simulation results that affects the averages creating a distorted image of the true scaling behavior.

In Fig. 4.16, the vertical fluxes are separated into SGS and resolved contributions for the hour between 2300-2400 LST. This figure is representative of all stable periods. The effect of the strongly stable conditions is manifested by a heavy burden placed on the SGS model, as signified by the large SGS flux contributions. The resolved contribution is extremely low in both momentum and potential temperature vertical flux in all simulations. Basu et al. [10] found similar results for this case with a resolution of 160^3 grid points. Although the formulation of these cases is LES, the simulation's performance could be interpreted more as quasi-RANS modeling instead of typical LES behavior. In a study done by Catalano and Cenedese [25], the diurnal cycle was simulated with LES in the presence of a valley. They used a stretched grid to increase resolution in the valley, where a cold pool formed at night with highly stable conditions. The results observed in the current study agree with those found by Catalano and Cenedese [25] in that increased vertical resolution does not provide sufficient improvement to resolve the small scale motions present under strongly stable conditions.

The AMR simulation does however provide some improvement at the points closest to the surface. In the lowest few points, the resolved contribution to the fluxes increases and is the simulation with largest resolved flux. The increase does not continue throughout the boundary layer and the benefit of AMR quickly subsides. It is interesting that the 96^3 static simulation has greater resolved momentum and sensible heat flux contributions between $z = 0.2H$ and $z = 0.4H$ (a trait observed in the middle and late stable periods). In all static simulations, the maximum momentum and sensible heat flux happens on the second and third LES nodes. Therefore, as a consequence of the coarser spacing for the 96^3 static simulation, the maximum flux occurs higher in the boundary layer. This indicates that the 96^3 simulation has generated enough unrealistic turbulence in the lowest levels, perhaps from the influence of the boundary condition, that the resolved scales can have more of an impact. Overall, the fluxes support the conclusion that horizontal refinement, along with potentially an even further increase in vertical resolution, is requisite to provide a more credible LES simulation of the diurnal cycle with strongly stable nocturnal conditions.

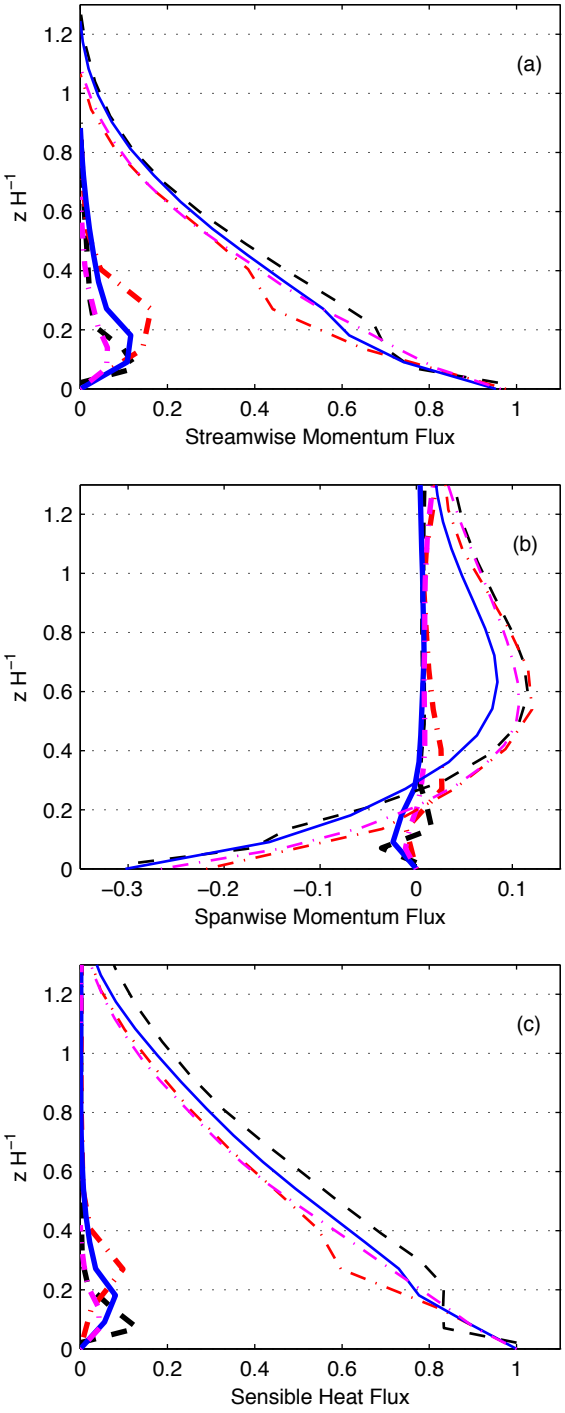

Figure 4.16. Comparison of SGS (thin lines) and resolved contributions (thick lines) to LES normalized momentum flux $u_{*L}^2 u_*^{-2}$ (a,b) and normalized sensible heat flux, $\langle w\theta \rangle \langle w\theta \rangle_0^{-1}$ (c) during the stable regime. Hourly average is between 2300-2400 LST. Line types are as follows: AMR (— —), 96^3 (– · –), 192^3 (——), $96 \times 96 \times 192$ (– · –).

CHAPTER 5

CONCLUSIONS

A diurnal cycle of the ABL has been simulated to examine the ability of LES enhanced with vertical AMR. The wide range of scales in the ABL and particularly the disparity between the large, turbulent motions of the CBL and the small scale, local turbulence of the SBL are computationally problematic in a simulation with one grid. Often, the SBL is left under-resolved for proper LES performance in favor of computational affordability. Therefore, vertical AMR has been implemented to allocate vertical grid spacing in critical regions during both the convective and stable regimes of a single diurnal simulation and maintain computational affordability. Resolutions of 96^3 static, 96^3 AMR, $96 \times 96 \times 192$, and 192^3 grid points were used to simulate the Wangara days 33-34 and analyze the technique.

During the day, vertical AMR clustered points near the surface providing improved resolution of the surface layer. Potential temperature and sensible heat flux profiles were particularly sensitive to the near ground resolution. This led to increased warming and subsequently a better match of the 192^3 simulation's first-order mean statistics throughout the CBL compared to the 96^3 static simulation. Second-order statistics also exhibited sensitivity to vertical resolution. Vertical variance of the AMR simulation more closely matched higher resolution results in the mixed layer. However, horizontal and potential temperature variances were generally insensitive in the mixed layer. In the entrainment zone, the AMR simulation provided a better match than the 96^3 static resolution for horizontal and potential temperature variances when compared to the 192^3 resolution simulation. Towards the ground however, the high aspect ratio of the AMR resulted in increased horizontal and potential temperature variances. Static grid simulations with increased vertical resolution but 96^2 points for the horizontal resolution produced very similar results confirming the impact of aspect ratio on near surface variance. Third-order statistics indicated that horizontal resolution has a strong impact on higher-order statistics. All three 96^2 horizontal points simulations produced very similar vertical velocity skewness, that all deviated from the higher resolution results. This indicates that increased vertical

resolution alone was not sufficient to drastically improve third-order moments.

During the night, vertical AMR clustered points in the SBL. The AMR simulation friction velocity and surface sensible heat flux matched high resolution simulations closer than the 96^3 and $96 \times 96 \times 192$ static grid simulations. Despite the increase of vertical resolution in the SBL, the SBL height was overestimated by both the AMR and $96 \times 96 \times 192$ simulations suggesting the importance of horizontal resolution in the representation of the SBL dynamics. The benefit of AMR in the SBL regime for first-order statistics was not as large as observed in the CBL regime. In the stable surface layer, increased vertical resolution improved the representation of mean wind speed and potential temperature profiles. Additionally, the total momentum and sensible heat fluxes from the AMR simulation matched the 192^3 simulation results better than 96^3 static simulation results in the surface layer. Above the surface layer, the improvements wane and the AMR and $96 \times 96 \times 192$ simulations no longer match the trends of the 192^3 resolution case. Generally, the low resolution simulations had a slower, more diffuse LLJ throughout the stable time period. However, in the late stable period the LLJ from the AMR simulation does had a faster mean wind speed that matched the 192^3 simulation better than the 96^3 and $96 \times 96 \times 192$ static simulations. Potential temperature profiles had a more gradual change into the residual layer and were warmer with height for the low resolution simulations compared to the high resolution simulation. There was also more total momentum and sensible heat flux above the surface layer in the lower resolution simulations than in the 192^3 simulation. The SGS and resolved contributions to the momentum and sensible heat flux profiles reveal that simulations could not sufficiently resolve the SBL in all simulations, even at the finest horizontal and vertical resolutions tested. This is an artifact of the strong stability of the case resulting in the majority of motions being smaller than the filter scale. Vertical AMR did provide slightly more resolved variance in the lower portion of the SBL, however the percentage of resolved to SGS contributions was still low. Even with this under resolution, first- and second-order statistics still show basic features of the SBL including positive curvature for potential temperature profiles and approximate local scaling for turbulent fluxes.

Overall, vertical AMR improves LES of the diurnal cycle. During the day, better representation throughout the CBL can be achieved at a greatly reduced computational cost. However, due to the stratification associated with the SBL (especially strongly stable situations), the benefit of the vertical AMR is limited. Near ground profiles can be improved at a lower cost than general increased resolution simulations and without

the need for *a priori* specification of vertical grid stretching. However, to provide a more accurate simulation, increased horizontal refinement is required. With only vertical resolution refinements, the LES has overly large SGS contributions limiting the fidelity of LES resolved statistics. Therefore, the next logical step to provide a highly affordable and accurate LES representation of the diurnal cycle, especially one with moderate to strongly stable conditions, is to provide horizontal AMR in combination with the vertical AMR explored in the study.

APPENDIX

AMR CRITERIA COMPARISON

Where a monitor function distributes resolution is critical to the success of any vertical AMR technique. Along with the monitor function used to obtain the results in the main body of this work, other criteria were tested to determine the performance of different AMR criteria for vertical AMR with LES of the ABL diurnal cycle.

Fig. A.1 depicts time height plots of the vertical spacing saved every 5 minutes of simulated time for three different monitor functions used in this study. Overlaid on these plots is the calculated boundary layer height for reference. The different monitor functions were all generated from Eq. (3.18) with varying values for the λ constants to provide increased resolution in areas of different focus. Table A.1 provides the constants and criteria focus of each function, labeled (a), (b), and (c). Fig. A.1a is the monitor function used in the main body of this paper. The focus of this criteria is to provide increased vertical resolution in areas of high shear and high vertical potential temperature gradients. The vertical potential temperature gradient is given extra weight with λ_2 to ensure resolution increase in the entrainment zone at the top of the CBL, as observed in Fig. A.1a. Low values of λ_2 resulted in only minor increases in resolution in the entrainment zone while larger values would cause the criteria to behave like criteria (c). The absolute temperature term in equation Eq. (3.18) (λ_3 term) was found to be important for two reasons. The first is that it provided a way to reduce unwanted effects from initial conditions that cause artificial, unrealistic gradients to be present outside of the initial CBL. In addition, the term also reduces unwanted clustering resultant from the remaining gradients at the top of residual layer long after the evening transition finishes. The unwanted effects are clearly present in Fig. A.1a and Fig. A.1b. However, the criteria has a slight drawback of a minor decrease in resolution within in the SBL compared to the other two criteria shown.

The focus of the monitor function represented in Fig. A.1b is to provide increased resolution only in areas of high shear. This criteria by itself provides increased resolution near the surface, in the entrainment zone, and in the SBL. However, the criteria undesirably

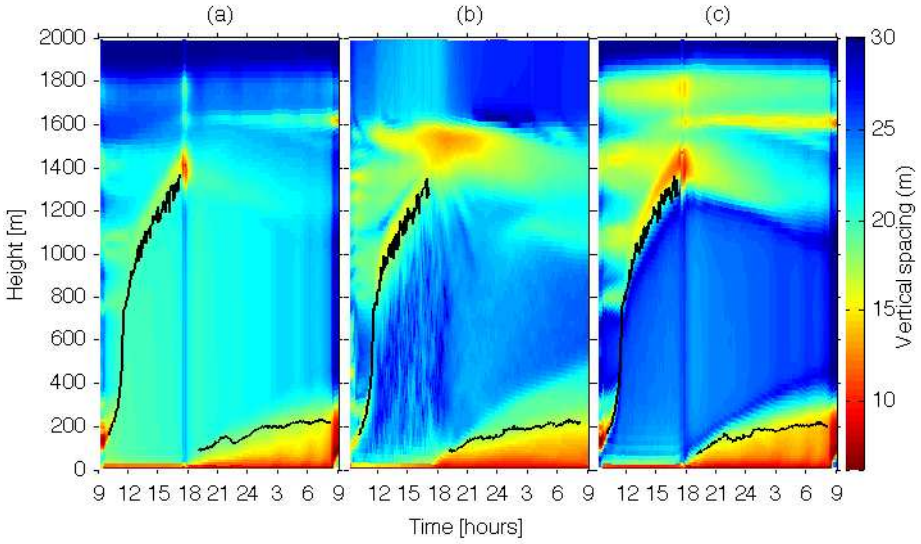

Figure A.1. Behavior of three different AMR criteria. Contour plots show vertical resolution (m) profiles saved every 5 minutes of physical time. Boundary layer heights are overlaid to show turbulence regimes. Criteria are detailed in Table A.1.

Table A.1. Details of AMR monitor functions from Eq. (3.18) for comparison study

Plot	λ_1	λ_2	λ_3	Focus
(a)	1	6	1	Velocity gradient Potential temperature gradient Potential temperature profile
(b)	1	0	0	Velocity gradient
(c)	0	1	0	Potential temperature gradient

allows resolution in the CBL that is coarser than the resolution in the sponge layer. In addition, leftover gradients at the top of the residual layer attract resolution away from the SBL at night. Fig. A.1c focuses on potential temperature gradients. Increased resolution is appropriately assigned near the surface and in the entrainment zone during the day, and in the SBL at night. Despite this positive behavior, the criteria suffers from effects of the initial conditions. Gradients from the initial conditions are introduced into the sponge layer, which are not mixed out and attract resolution throughout the simulation. This criteria also attracts resolution at the top of the residual layer in a way similar to the monitor function of Fig. A.1b.

A.1 Criteria sensitivity

The differences in behavior of the three criteria of Fig. A.1 had noticeable impact on some results, while other results were relatively insensitive to the adaptive criteria. The convective BLH and surface fluxes, as presented in Fig. A.2, were generally unaffected by the grid spacing. The only noticeable difference is observed in the surface sensible heat flux, plot (b), at approximately 1200. The criteria of Fig. A.1c has the largest spike in sensible heat flux, which is attributed to the second LES node being closer to ground in this simulation than the simulations of Fig. A.1a and b. As a result, the air temperature is warmer in the simulation with the criteria of Fig. A.1c than the other two simulations, as observed in Fig. A.3a. By the same logic, the criteria of Fig. A.1b is the coolest of the three simulations suggesting the importance of the surface layer, and not just the first LES node. Fig. A.3b depicts the normalized sensible heat flux in the entrainment zone. Following similar reasoning, the simulation with the criteria from Fig. A.1a does not match the higher resolution simulation as well as the other two criteria simulations. Both of the simulations from the criteria of Fig. A.1b and c have a higher concentration of points due to the effect of high gradients in this region that have not been diluted by the absolute temperature criteria, the last term in Eq. (3.18). The total horizontal and vertical velocity variances also have a dependence on the monitor function criteria. The simulation with the criteria of Fig. A.1b does not always resemble that of the other two AMR simulations. In Fig. A.4a, the total horizontal variance in the entrainment zone is the largest with the criteria of Fig. A.1b. In Fig. A.4b, the criteria of Fig. A.1b has the lowest average total vertical velocity variance of the three simulations.

The surface fluxes at night indicate higher sensitivity to the grid spacing than observed during the convective regime, especially in the early hours of the stable regime as presented

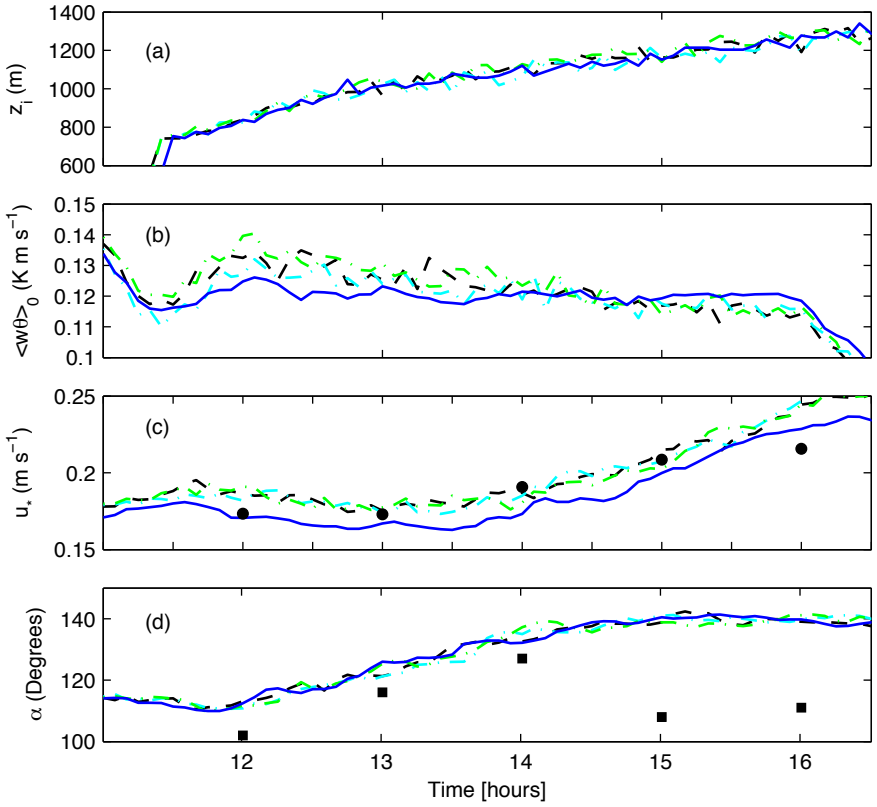

Figure A.2. Comparisons of the LES time series of boundary layer height, z_i (a), surface sensible heat flux, $\langle w\theta \rangle_0$ (b), surface friction velocity, u_* (c), and wind direction, α (d) with corresponding Clarke data ($C71_0$). Line types are as follows: criteria (a) (— —), criteria (b) (– · –), criteria (c) (– · –), 192^3 (——). H81(▪), $C71_0$(•).

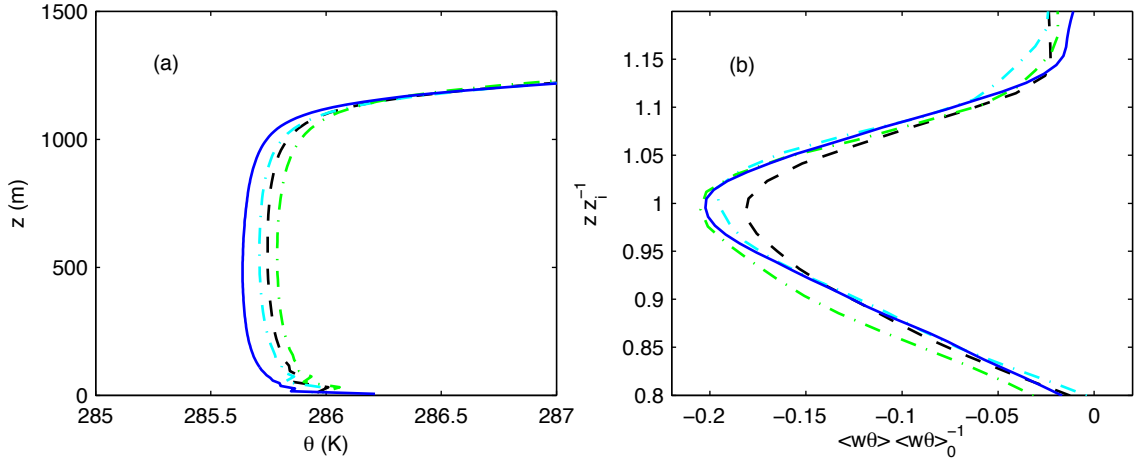

Figure A.3. Comparison of LES potential temperature, θ (a) and non-dimensional sensible heat flux $\langle w\theta \rangle \langle w\theta \rangle_0^{-1}$ (b) during the stable regime between 1400-1500 LST. Line types are as follows: criteria (a) (— —), criteria (b) (– · –), criteria (c) (– · –), 192^3 (——).

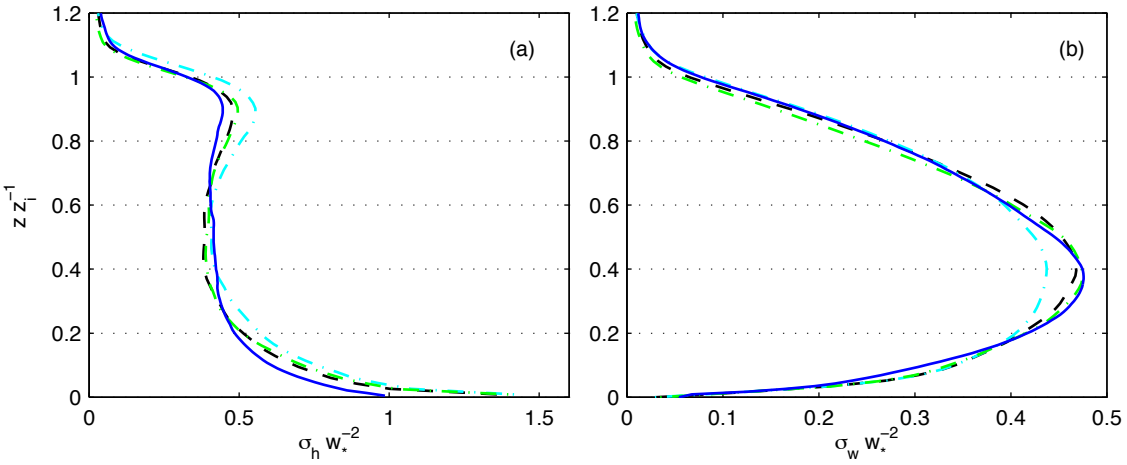

Figure A.4. CComparison of LES total horizontal variances $\sigma_h w_*^{-1}$ (a) and vertical variance $\sigma_w w_*^{-1}$ (b) during the convective regime between 1500-1600 LST. Line types are as follows: criteria (a) (– –), criteria (b) (– · –), criteria (c) (– · –), 192^3 (——).

in Fig. A.5. The surface sensible heat flux and u_* exhibit the most difference before 2400. Since the criteria of Fig. A.1b and c both react very similar to one another, and the criteria of Fig. A.1a deviates from them, one possible explanation is attributed to the difference of spacing in the early hours between 1800-2400 LST. During this period the criteria of Fig. A.1a results in fewer points in the lowest 200 m. Away from the surface, the sensible heat flux exhibited the most sensitivity to the different criteria. Fig. A.6 is provided for the middle period of the stable regime which had the most sensitivity between the simulations in the lower 400 m. Differences in results were less prevalent during the early and late stable periods.

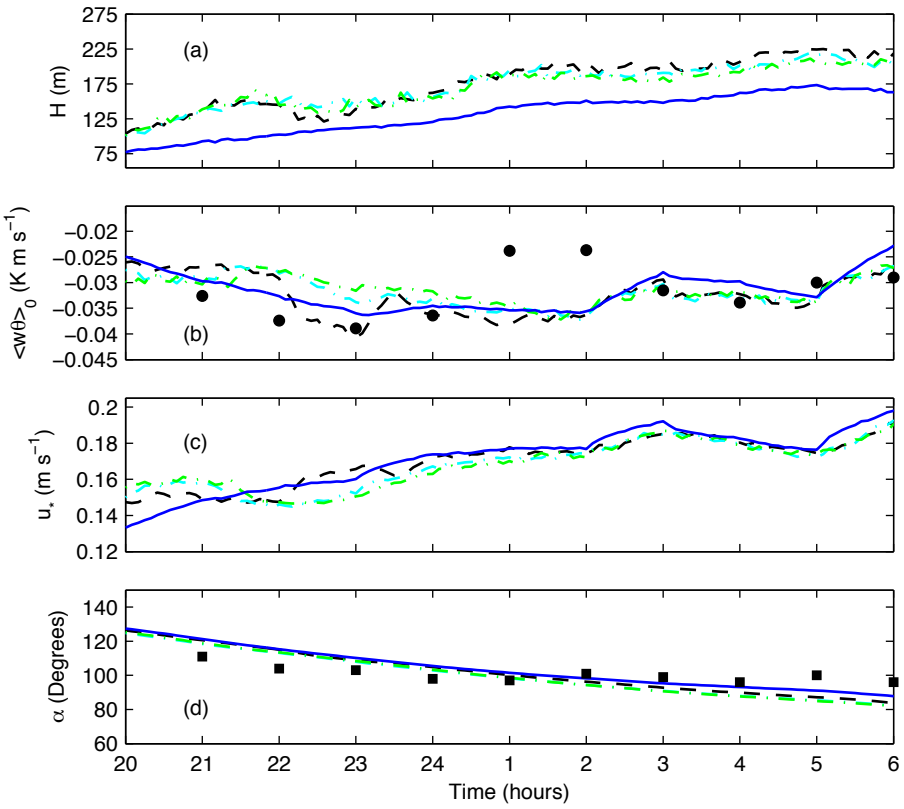

Figure A.5. Comparisons of the LES time series for the stable regime of boundary layer height, H (a), surface sensible heat flux, $\langle w\theta \rangle_0$ (b), surface friction velocity, u_* (c), Obukhov length, and near surface wind direction, α with corresponding Clarke data $C71_0$. Line types are as follows: criteria (a) (— —), criteria (b) (– · –), criteria (c) (– · · –), 192^3 (——). H81(▪), $C71_0$(•).

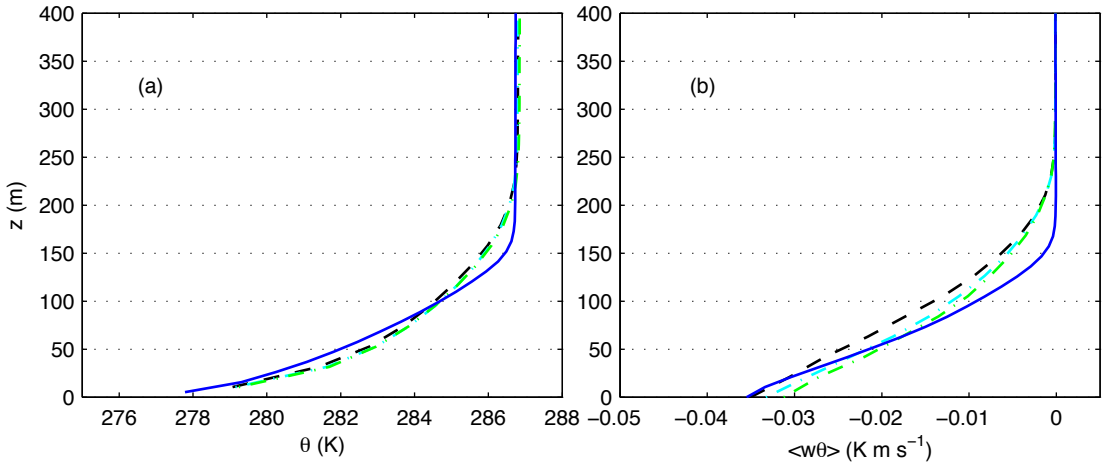

Figure A.6. Comparison of LES potential temperature, θ (a) and sensible heat flux $\langle w\theta \rangle$ (b) during the stable regime between 2300-2400 LST. Line types are as follows: criteria (a) (— —), criteria (b) (– · –), criteria (c) (– · –), 192^3 (——).

REFERENCES

[1] J. D. Albertson, "Large-eddy simulation of land-atmosphere interaction," Ph.D. dissertation, University of California, Davis, Davis One Shields Avenue Davis, CA 95616, 1996.

[2] A. S. Almgren, J. B. Bell, P. Colella, L. H. Howell, and M. L. Welcome, "A conservative adaptive projection method for the variable density incompressible navier-stokes equations," *J. Comp. Phys.*, vol. 142, pp. 1–46, 1998.

[3] A. Andrén, "The structure of stably stratified atmospheric boundary layers: A large-eddy simulation study," *Quart. J. Roy. Meteorol. Soc.*, vol. 121, pp. 961–985, 1995.

[4] E. Aristodemou, T. Bentham, C. Pain, R. Colvile, A. Robins, and H. ApSimon, "A comparison of mesh-adaptive les with wind tunnel data for flow past buildings: Mean flows and velocity fluctuations," *Atmos. Environ.*, vol. 43, pp. 6238–6253, 2009.

[5] S. P. Arya, *Introduction to Micrometeorology*, 2nd ed. San Diego: Academic Press, 2001.

[6] I. Babuska, "The selfadaptive approach in the finite element method, the mathematics of finite elements and applications," in *Proceedings of the Brunel University Conference of the Institute of Mathematics and its Applications held in April 1975*, 1976, pp. 125–142.

[7] D. P. Bacon, N. N. Ahmad, Z. Boybeyi, T. J. Dunn, M. S. Hall, P. C. S. Lee, R. A. Sarma, M. D. Turner, K. T. Waight, S. H. Young, and J. W. Zack, "A dynamically adapting weather and dispersion model: The operational multiscale environment model with grid adaptivity (omega)," *mwr*, vol. 128, p. 2044, 2000.

[8] S. Basu, A. A. M. Holtslag, and F. C. Bosveld, "Gabls3-les intercomparison study," in *Workshop on Diurnal cycles and the stable boundary layer, 7-10 November 2011*, ser. 5.5. Shinfield Park, Reading: ECMWF, 2012, pp. 75–82.

[9] S. Basu, A. A. M. Holtslag, B. J. H. van de Wiel, A. F. Moene, and G.-J. Steeneveld, "An inconvenient "truth" about using sensible heat flux as a surface boundary condition in models under stably stratified regimes," *Acta Geophysica*, vol. 56, pp. 88–99, Mar 2008.

[10] S. Basu, J.-F. Vinuesa, and A. Swift, "Dynamic les modeling of a diurnal cycle," *J. Appl. Meteorol.*, vol. 47, pp. 1156–1174, 2007, dOI 10.1175/2007JAMC1677.1.

[11] S. Basu, F. Porté-Agel, E. Foufoula-Georgiou, J.-F. Vinuesa, and M. Pahlow, "Revisiting the local scaling hypothesis in stably stratified atmospheric boundary-layer turbulence: An integration of field and laboratory measurements with large-eddy simulations," *Boundary-Layer Meteorol.*, vol. 119, pp. 473–500, 2006, dOI 10.1007/s10546-005-9036-2.

[12] R. J. Beare, "The role of shear in the morning transition boundary layer," *Boundary-Layer Meteorol.*, vol. 129, pp. 395–410, 2008, dOI 10.1007/s10546-008-9324-8.

[13] R. J. Beare, J. M. Edwards, and A. J. Lapworth, "Simulation of the observed evening transition and nocturnal boundary layers: Large-eddy simulation," *Quart. J. Roy. Meteorol. Soc.*, vol. 118, pp. 247–272, 2006, dOI 10.1007/s10546-004-2820-6.

[14] R. J. Beare and M. K. MacVean, "Resolution sensitivity and scaling of large-eddy simulations of the stable boundary layer," *Boundary-Layer Meteorol.*, vol. 112, pp. 257–281, 2004.

[15] R. J. Beare, M. K. MacVean, A. A. M. Holtslag, J. Cuxart, I. Esau, J.-C. Golaz, M. A. Jimenez, M. Khairoutdinov, B. Kosovic, D. Lewellen, T. S. Lund, J. K. Lundquist, A. McCabe, A. F. Moene, Y. Noh, S. Raasch, and P. Sullivan, "An intercomparison of large-eddy simulations of the stable boundary layer," *Boundary-Layer Meteorol.*, vol. 118, pp. 247–272, 2006, dOI 10.1007/s10546-004-2820-6.

[16] J. Behrens, *Adaptive atmospheric modeling : key techniques in grid generation, data structures, and numerical operations with applications*. Springer Berlin Heidelberg, 2006.

[17] M. Berger and J. Oliger, "Adaptive mesh refinement for hyperbolic partial differential equations," *J. Comp. Phys.*, vol. 53, pp. 484–512, 1984, dOI 10.1016/0021-9991(84)90073-1.

[18] J. U. Brackbill and J. S. Saltzman, "Adaptive zoning for singular problems in two dimensions," *J. Comp. Phys.*, vol. 46, pp. 342–368, 1982.

[19] A. R. Brown, R. T. Cederwall, A. Chlond, P. G. Duynkerke, J.-C. Golaz, M. Khairoutdinov, D. C. Lewellen, A. P. Lock, M. K. MacVean, C.-H. Moeng, R. A. J. Neggers, A. P. Siebesma, and B. Stevens, "Large-eddy simulation of the diurnal cycle of shallow cumulus convection over land," *Quart. J. Roy. Meteorol. Soc.*, vol. 128, no. 582, pp. 1075–1093, 2002.

[20] A. R. Brown, S. H. Derbyshire, and P. J. Mason, "Large-eddy simulation of stable atmospheric boundary layers with a revised stochastic subgrid model," *Quart. J. Roy. Meteorol. Soc.*, vol. 120, pp. 1485–1512, 1994.

[21] C. J. Budd, W. Huang, and R. Russell, "Adaptivity with moving grids," *Acta Num.*, vol. 18, pp. 111–241, 2009.

[22] H. Burchard, "Non-uniform adaptive vertical grids in one-dimensional numerical ocean models," *Ocean Mod.*, vol. 6, pp. 51–81, 2004.

[23] H. Burchard, O. Petersen, and O. Petersen, "Hybridization between - and z-coordinates for improving the internal pressure gradient calculation in marine models with steep bottom slopes," *Int. Jo. Num. Met. Fluids*, vol. 25, pp. 1003–1023, Nov 1997.

[24] P. Caldwell and C. S. Bretherton, "Large eddy simulation of the diurnal cycle in southeast pacific stratocumulus," *J. Atmos. Sci.*, vol. 66, p. 432, 2009.

[25] F. Catalano and A. Cenedese, "High-resolution numerical modeling of thermally driven slope winds in a valley with strong capping," *J. Appl. Meteorol. Clim.*, vol. 49, pp. 1859–1880, 2010.

[26] J. G. Charney, "Some remaining problems in numerical weather prediction," *Adv. Num. Wea. Pred.*, pp. 61–70, 1966.

[27] A. Cheng, K.-M. Xu, and B. Stevens, "Effects of resolution on the simulation of boundary-layer clouds and the partition of kinetic energy to subgrid scales," *Jo. Adv. Mod. Earth Sys.*, vol. 2, p. 3, Feb 2010.

[28] R. H. Clarke, A. J. Dyer, R. R. Brook, D. G. Reid, and A. J. Troup, "The wangara experiment: Boundary layer data," Division of Meteorological Physics, Tech. Rep. 19, 1971.

[29] A. W. Cook, "A consistent approach to large eddy simulation using adaptive mesh refinement," *J. Comp. Phys.*, vol. 154, pp. 117 – 133, 1999.

[30] J. Cuxart, A. A. M. Holtslag, R. J. Beare, E. Bazile, A. Beljaars, A. Cheng, L. Conangla, M. Ek, F. Freedman, R. Hamdi, A. Kerstein, H. Kitagawa, G. Lenderink, D. Lewellen, J. Mailhot, T. Mauritsen, V. Perov, G. Schayes, G.-J. Steeneveld, G. Svensson, P. Taylor, W. Weng, S. Wunsch, and K.-M. Xu, "Single-column model intercomparison for a stably stratified atmospheric boundary layer," *Boundary-Layer Meteorol.*, vol. 118, pp. 273–303, 2006, dOI 10.1007/s10546-005-3780-1.

[31] J. W. Deardorff, "Numerical investigation of neutral and unstable planetary boundary layers," *J. Atmos. Sci.*, vol. 29, pp. 91–115, 1972.

[32] ——, "Three-dimensional numerical study of the height and mean structure of a heated planetary boundary layer," *Boundary-Layer Meteorol.*, vol. 7, pp. 81–106, 1974.

[33] ——, "Three-dimensional numerical study of turbulence in an entraining mixed layer," *Boundary-Layer Meteorol.*, vol. 7, p. 199226, 1974.

[34] G. Degrazia, U. Rizza, F. Puhales, A. Goulart, J. Carvalho, G. Welter, and E. Marques Filho, "A variable mesh spacing for large-eddy simulation models in the convective boundary layer," *Boundary-Layer Meteorol.*, vol. 131, pp. 277–292, 2009, dOI 10.1007/s10546-009-9360-z.

[35] G. S. Dietachmayer and K. K. Droegemeier, "Application of continuous dynamic grid adaptation techniques to meteorological modeling. i : Basic formulation and accuracy," *Mon. Weat. Rev.*, vol. 120, pp. 1675–1706, 1992.

[36] T. Dunbar, E. Hanert, and R. Hogan, "A one-dimensional finite-element boundary-layer model with a vertical adaptive grid," *Boundary-Layer Meteorol.*, vol. 74, pp. 459–472, 2008.

[37] J. H. Ferziger and M. Perić, *Computational Methods for Fluid Dynamics*, 3rd ed. Springer, 2002.

[38] B. H. Fiedler, "Grid adaption and its effect on entrainment in an e l model of the atmospheric boundary layer," *mwr*, vol. 130, pp. 733–740, 2002.

[39] B. H. Fiedler and R. J. Trapp, "A fast dynamic grid adaption scheme for meteorological flows," *mwr*, vol. 121, pp. 2879–2888, 1993.

[40] V. K. Garg, *Applied Computational Fluid Dynamics*. New York, New York: Marcel Dekker, Inc., 1998.

[41] P. A. Gnoffo, "A finite-volume, adaptive grid algorithm applied to planetary entry flowfields," *aiaa*, vol. 21, pp. 1249–1254, 1983.

[42] D. E. Goldstein and O. V. Vasilyev, "Stochastic coherent adaptive large eddy simulation method," *Phys. Fluids*, vol. 16, pp. 2497–2513, Jul. 2004.

[43] A. Goulart, B. Bodmann, M. de Vilhena, P. Soares, and D. Moreira, "On the time evolution of the turbulent kinetic energy spectrum for decaying turbulence in the convective boundary layer," *Boundary-Layer Meteorol.*, vol. 138, pp. 61–75, 2010.

[44] A. Goulart, G. Degrazia, U. Rizza, and D. Anfossi, "A theoretical model for the study of convective turbulence decay and comparison with large-eddy simulation data," *Boundary-Layer Meteorol.*, vol. 107, pp. 143–155, 2003.

[45] D. F. Hawken, J. J. Gottlieb, and J. S. Hansen, "Review of some adaptive node-movement techniques in finite-element and finite-difference solutions of partial differential equations," *J. Comp. Phys.*, vol. 95, pp. 254–302, Aug 1991.

[46] B. B. Hicks, "An analysis of wangara micrometeorology: Surface stress, sensible heat, evaporation, and dewfall," *NOAA Tech. Memo.*, vol. ERL ARL-104, p. 36, 1981.

[47] R. Hofmeister, H. Burchard, and J.-M. Beckers, "Non-uniform adaptive vertical grids for 3d numerical ocean models," *Ocean Mod.*, vol. 33, pp. 70–86, 2010.

[48] T. W. Horst, J. Kleissl, D. H. Lenschow, C. Meneveau, C.-H. Moeng, M. B. Parlange, P. P. Sullivan, and J. C. Weil, "Hats: Field observations to obtain spatially filtered turbulence fields from crosswind arrays of sonic anemometers in the atmospheric surface layer," *J. Atmos. Sci.*, 2004, dOI 10.1175/1520-0469(2004)061¡1566:HFOTOS¿2.0.CO;2.

[49] W. Huang and R. D. Russell, *Adaptive Moving Mesh Methods*. New York: Springer, 2011, vol. 174.

[50] M. E. Hubbard and N. Nikiforakis, "A three-dimensional, adaptive, godunov-type model for global atmospheric flows," *Mon. Weat. Rev.*, vol. 131, pp. 1848–1864, 2003.

[51] J. P. Iselin, W. J. Gutowski, and J. M. Prusa, "Tracer advection using dynamic grid adaptation and mm5," *mwr*, vol. 133, p. 175, 2005.

[52] J. P. Iselin, J. M. Prusa, and W. J. Gutowski, "Dynamic grid adaptation using the mpdata scheme," *mwr*, vol. 130, p. 1026, 2002.

[53] M. A. Jimenez and J. Cuxart, "Large-eddy simulations of the stable boundary layer using the standard Kolmogorov theory: Range of applicability," *Boundary-Layer Meteorol.*, vol. 115, pp. 241–261, 2005.

[54] S. Khanna and J. G. Brasseur, "Analysis of monin obukhov similarity from large-eddy simulation," *J. Fluid Mech.*, vol. 345, pp. 254–286, 1997.

[55] S. B. Kim, K. Yamaguchi, A. Kondo, and S. Soda, "A comparative study of the melloryamada and $k-\epsilon$ two-equation turbulence models in atmospheric application," *J. Wind Eng. Ind. Aerodyn.*, vol. 91, pp. 791–806, 2003.

[56] J. Kleissl, M. B. Parlange, and C. Meneveau, "Field experimental study of dynamic smagorinsky models in the atmospheric surface layer," *J. Atmos. Sci.*, vol. 61, pp. 2296–2307, 2004.

[57] B. Kosovic and J. A. Curry, "A large eddy simulation study of a quasi-steady, stably stratified atmospheric boundary layer," *J. Atmos. Sci.*, vol. 57, pp. 1052–1068, 2000.

[58] A. G. Kravchenko, P. Moin, and K. Shariff, "B-spline method and zonal grids for simulations of complex turbulent flows," *J. Comp. Phys.*, vol. 151, pp. 757–789, may 1999.

[59] V. Kumar, J. Kleissl, C. Meneveau, and M. B. Parlange, "Large-eddy simulation of a diurnal cycle of the atmospheric boundary layer: Atmospheric stability and scaling issues," *Water Resources Res.*, vol. 42, p. W06D09, 2006.

[60] V. Kumar, G. Svensson, A. A. M. Holtslag, C. Meneveau, and M. B. Parlange, "Impact of surface flux formulations and geostrophic forcing on large-eddy simulations of diurnal atmospheric boundary layer flow," *jamc*, vol. 49, pp. 1496–1516, Jul 2010.

[61] R. J. LeVeque, *Finite Volume Methods for Hyperbolic Problems*. Cambridge University Press, 2002.

[62] D. C. Lewellen and W. S. Lewellen, "Large-eddy boundary layer entrainment," *J. Atmos. Sci.*, vol. 55, pp. 2645–2665, 1998.

[63] R. Marchand and T. Ackerman, "A cloud-resolving model with an adaptive vertical grid for boundary layer clouds," *J. Atmos. Sci.*, vol. 68, pp. 1058–1074, 2011.

[64] P. J. Mason, "Large-eddy simulation of the convective atmospheric boundary layer," *J. Atmos. Sci.*, vol. 46, pp. 1492–1516, 1989.

[65] P. J. Mason and N. S. Callen, "On the magnitude of the subgrid-scale eddy coefficient in large-eddy simulations of turbulent channel flow," *J. Fluid Mech.*, vol. 162, pp. 439–462, 1986.

[66] P. J. Mason and S. H. Derbyshire, "Large-eddy simulation of the stably-stratified atmospheric boundary layer," *Boundary-Layer Meteorol.*, vol. 53, pp. 117–162, 1990.

[67] S. M. Mitran, "A comparison of adaptive mesh refinement approaches for large eddy simulation," in *Aug Washington Univ Seattle Dept of Applied Mathematics*, 2001, p. 12.

[68] C.-H. Moeng, J. Dudhia, J. Klemp, and P. Sullivan, "Examining Two-Way Grid Nesting for Large Eddy Simulation of the PBL Using the WRF Model," *Mon. Weat. Rev.*, vol. 135, p. 2295, 2007.

[69] C.-H. Moeng, "A large-eddy-simulation model for the study of planetary boundary-layer turbulence," *J. Atmos. Sci.*, vol. 41, pp. 2052–2062, 1984.

[70] K. Nakahashi and G. S. Deiwert, "A practical adaptive-grid method for complex fluid-flow problems," in *Ninth International Conference on Numerical Methods in Fluid Dynamics*, ser. Lecture Notes in Physics, Soubbaramayer and J. Boujot, Eds., vol. 218. Springer Berlin / Heidelberg, 1985, pp. 422–426.

[71] ——, "Self-adaptive-grid method with application to airfoil flow," *aiaa*, vol. 25, pp. 513–520, 1987.

[72] A. Naudin, L. Vervisch, and P. Domingo, "A turbulent-energy based mesh refinement procedure for large eddy simulation," in *Advances in Turbulence XI*, ser. Springer Proceedings in Physics, vol. 117, 2007, pp. 413–415.

[73] F. T. M. Nieuwstadt, "The turbulent structure of the stable, nocturnal boundary layer," *J. Atmos. Sci.*, vol. 41(14), pp. 2202–2216, 1984.

[74] F. T. M. Nieuwstadt and R. A. Brost, "The decay of convective turbulence," *J. Atmos. Sci.*, vol. 43, pp. 532–546, 1986.

[75] F. T. M. Nieuwstadt, P. J. Mason, C.-H. Moeng, and U. Schumann, "Large-eddy simulation of the convective boundary layer: A comparison of four computer codes," in *Turbulent Shear Flows 8*, F. Durst, R. Friedrich, B. E. Launder, F. W. Schmidt, U. Schumann, and J. H. Whitelaw, Eds. Springer, 1991, pp. 343–367.

[76] C. Pantano, R. Deiterding, D. J. Hill, and D. I. Pullin, "A low numerical dissipation patch-based adaptive mesh refinement method for large-eddy simulation of compressible flows," *J. Comp. Phys.*, vol. 221, pp. 63–87, Jan 2007.

[77] D. Pino, H. Jonker, J. Arellano, and A. Dosio, "Role of shear and the inversion strength during sunset turbulence over land: Characteristic length scales," *Boundary-Layer Meteorol.*, vol. 121, pp. 537–556, 2006.

[78] G. S. Poulos, W. Blumen, D. C. Fritts, J. K. Lundquist, J. Sun, S. P. Burns, C. Nappo, R. Banta, R. Newsom, J. Cuxart, E. Terradellas, B. Balsley, and M. Jensen, "Cases-99: A comprehensive investigation of the stable nocturnal boundary layer." *bams*, vol. 83, pp. 555–581, Apr 2002.

[79] N. Ramanathan, K. Srinivasan, and B. V. Seshasayee, "Averaging procedures for flow within vegetation canopies," *J. Appl. Meteorol.*, vol. 34, pp. 542–548, 1995.

[80] U. Rizza, M. M. Miglietta, O. C. Acevedo, V. Anabor, G. A. Degrazia, A. G. Goulart, and H. R. Zimmerman, "Large-eddy simulation of the planetary boundary layer under baroclinic conditions during daytime and sunset turbulence," *Meteorol. Applic.*, 2012.

[81] P. Sagaut, *Large Eddy Simulation for Incompressible flows: An Introduction*, 2nd ed. Berlin Heidelberg: Springer-Verlag, 2002.

[82] E. M. Saiki, C.-H. Moeng, and P. P. Sullivan, "Large-eddy simulation of the stably stratified planetery boundary layer," *Boundary-Layer Meteorol.*, vol. 95, pp. 1–30, 2000.

[83] F. Schimmel, "Development and test of an atmospheric flow model employing adaptive numerical methods," Ph.D. dissertation, Hamburg University, Germany, 2002.

[84] H. Schmidt and U. Schumann, "Coherent structure of the convective boundary layer derived from large-eddy simulations," *J. Fluid Mech.*, vol. 200, pp. 511–562, Mar 1989.

[85] D. J. Seidel, C. O. Ao, and K. Li, "Estimating climatological planetary boundary layer heights from radiosonde observations: Comparison of methods and uncertainty analysis," *Journal of Geophysical Research (Atmospheres)*, vol. 115, no. D14, p. 16113, aug 2010.

[86] W. C. Skamarock and J. B. Klemp, "Adaptive grid refinement for two-dimensional and three-dimensional nonhydrostatic atmospheric flow," *Mon. Weat. Rev.*, vol. 121, pp. 788–804, 1993.

[87] Z. Sorbjan, "Decay of convective turbulence revisited," *Boundary-Layer Meteorol.*, vol. 82, pp. 503–517, 1997.

[88] ——, "A numerical study of daily transitions in the convective boundary layer," *Boundary-Layer Meteorol.*, vol. 123, pp. 365–383, 2007.

[89] R. K. Srivastava, D. S. McRae, and M. T. Odman, "An adaptive grid algorithm for air-quality modeling," *J. Comp. Phys.*, vol. 165, pp. 437–472, 2000.

[90] A. V. Starchenko and A. S. Karyakin, "Simulation of turbulent transport during 24-hour evolution of the atmospheric boundary layer," in *Seventh International Symposium on Atmospheric and Ocean Optics*, 2000, pp. 626–633.

[91] B. Stevens, C.-H. Moeng, and P. P. Sullivan, "Large-eddy simulations of radiatively driven convection: Sensitivities to the representation of small scales." *J. Atmos. Sci.*, vol. 56, pp. 3963–3984, Dec 1999.

[92] D. E. Stevens and C. S. Bretherton, "Effects of resolution on the simulation of stratocumulus entrainment," *Quart. J. Roy. Meteorol. Soc.*, vol. 125, pp. 425–439, 1999.

[93] R. Stoll and F. Porté-Agel, "Dynamic subgrid-scale models for momentum and scalar fluxes in large-eddy simulations of neutrally stratified atmospheric boundary layers over heterogeneous terrain," *Water Resources Res.*, vol. 42, p. W01409, 2006.

[94] ——, "Effect of roughness on surface boundary conditions for large-eddy simulation," *Boundary-Layer Meteorol.*, vol. 118, pp. 169–187, 2006.

[95] ——, "Large-eddy simulation of the stable atmospheric boundary layer using dynamic models with different averaging schemes," *Boundary-Layer Meteorol.*, vol. 126, pp. 1–28, 2008.

[96] R. B. Stull, *An Introduction to Boundary Layer Meteorology.* Dordrecht: Kluwer Academic Publishers, 1988.

[97] P. P. Sullivan, C.-H. Moeng, B. Stevens, D. H. Lenschow, and S. D. Mayor, "Structure of the entrainment zone capping the convective atmospheric boundary layer," *J. Atmos. Sci.*, vol. 55, pp. 3042–3064, 1998.

[98] P. P. Sullivan and E. G. Patton, "The effect of mesh resolution on convective boundary layer statistics and structures generated by large-eddy simulation," *J. Atmos. Sci.*, vol. 68, pp. 2395–2415, 2011.

[99] G. Svensson, A. Holtslag, V. Kumar, T. Mauritsen, G. Steeneveld, W. Angevine, E. Bazile, A. Beljaars, E. de Bruijn, A. Cheng, L. Conangla, J. Cuxart, M. Ek, M. Falk, F. Freedman, H. Kitagawa, V. Larson, A. Lock, J. Mailhot, V. Masson, S. Park, J. Pleim, S. Sderberg, W. Weng, and M. Zampieri, "Evaluation of the diurnal cycle in the atmospheric boundary layer over land as represented by a variety of single-column models: The second gabls experiment," *Boundary-Layer Meteorol.*, vol. 140, pp. 177–206, 2011.

[100] R. I. Sykes and D. S. Henn, "Large-eddy simulation of turbulent sheared convection," *J. Atmos. Sci.*, vol. 46, pp. 1106–1118, 1989.

[101] J. R. Taylor, S. Sarkar, and V. Armenio, "Large eddy simulation of stably stratified open channel flow," *Phys. Fluids*, vol. 17, p. 116602, 2005.

[102] J. F. Thompson, "A survey of dynamically-adaptive grids in the numerical solution of partial differential equations," *Appl. Num. Math.*, vol. 1, pp. 3–27, 1985.

[103] A. Tomlin, M. Berzins, J. Ware, J. Smith, and M. J. Pilling, "On the use of adaptive gridding methods for modelling chemical transport from multi-scale sources," *Atmos. Environ.*, vol. 31, pp. 2945–2959, 1997.

[104] H. Xiao, C.-M. Wu, and C. R. Mechoso, "Buoyancy reversal, decoupling and the transition from stratocumulus to shallow cumulus topped marine boundary layers," *Clim. Dyn.*, vol. 37, pp. 971–984, Sep 2011.

[105] M. Xue, J. Zong, and K. K. Drogemeier, "Parameterization of pbl turbulence in a multi-scale nonhydrostatic model. preprints." ser. 11^{th} Conference on Numerical Weather Prediction. VA: Amer. Meteor. Soc., 1996, p. P2.5.

[106] T. Yamada and G. Mellor, "A simulation of the wangara atmospheric boundary layer data," *J. Atmos. Sci.*, vol. 32, pp. 2309–2329, 1975.

[107] B. Zhang, T. Wang, C. GU, and Z. DAI, "An adaptive control strategy for proper mesh distribution in large eddy simulation," *J. of Hydrod.*, vol. 22, pp. 865–870, 2010.

[108] O. Zienkiewicz, R. Taylor, and P. Nithiarasu, *The Finite Element Method.* Elsevier/Butterworth-Heinemann, 2005.